

Gravitational Wave Signatures of Primordial Black Hole Reheating in Upcoming Interferometry Missions

Debarun Paul,^a Md Riajul Haque^a and Supratik Pal^a

^a *Physics and Applied Mathematics Unit, Indian Statistical Institute, 203 B.T. Road, Kolkata 700108, India*

E-mail: debarun31paul@gmail.com, riaj.0009@gmail.com,
supratik@isical.ac.in

ABSTRACT: We investigate the prospects of detecting a stochastic gravitational wave (GW) background from the primordial black hole (PBH) reheating epoch. If PBHs form during a non-standard cosmological phase prior to the radiation-dominated era, they can dominate the Universe's energy density before evaporating via Hawking radiation. Such PBHs can generate induced GWs that may fall within the detectable range of future interferometry missions: (i) through isocurvature perturbations arising from the inhomogeneous spatial distribution of PBHs, and (ii) through the amplification of adiabatic perturbations triggered by the abrupt transition from PBH domination to radiation domination. We assess the detection prospects of such GW spectra using the signal-to-noise ratio, Fisher forecast analysis, and Markov chain Monte Carlo analysis with mock data from LISA and ET. Our findings reveal that ET exhibits superior sensitivity to both isocurvature- and adiabatic-induced GWs, covering a wide PBH mass range of $M_{\text{in}} \in (0.5 - 4 \times 10^7)$ g. However, we find that the relative uncertainties associated with the parameter of the isocurvature source are quite high. LISA, by contrast, is mostly sensitive to the adiabatic source, with $M_{\text{in}} \in (2 \times 10^4 - 5 \times 10^8)$ g. The combined effect of adiabatic and isocurvature sources on ET and LISA provides a multi-stage window into the post-inflationary Universe by constraining PBH mass, energy fraction, and the background equation of state.

Contents

1	Introduction	2
2	Brief overview of the primordial black hole reheating	3
3	Steps to investigate detection prospects in interferometry missions	6
3.1	Signal-to-noise ratio for different detectors	6
3.2	Statistical analysis with likelihood function	7
4	Gravitational waves from PBH reheating	8
4.1	Gravitational waves induced by isocurvature fluctuations	9
4.1.1	Statistical analysis in the light of the detectors	11
4.2	Gravitational waves induced by adiabatic fluctuations	14
4.2.1	Statistical analysis in the light of the detectors	17
5	Combined analysis with primordial source and PBH domination	19
5.1	Statistical analysis in the light of the detectors	21
6	Summary and outlook	27
A	Noise modelling	29
B	Calculation of cutoff function	30

1 Introduction

Primordial Black Holes (PBHs) can form from high-density fluctuations in the early Universe [1–3], offering insights into dark matter, cosmology, and gravitational wave (GW) sources. Unlike astrophysical black holes, which originate from the final stages of stellar evolution, PBHs can span a wide range of masses depending on the formation epoch and the underlying cosmology. The study of PBHs has received considerable interest in recent years, as they offer novel eyes to look into various aspects of the early Universe, including inflationary dynamics, dark matter, baryogenesis, and non-standard reheating scenarios. Recent observations of GWs by LIGO-Virgo collaboration [4–9], along with the growing interest in exploring dark matter candidates and early Universe cosmology, have made the studies of PBHs a timely one, as they could potentially account for a fraction of dark matter or leave imprints on stochastic GW backgrounds. Thus, any signature of PBHs in upcoming detectors could provide a powerful probe of the primordial Universe and dark matter, potentially unravelling new physics beyond the standard cosmological paradigm.

The formation of PBHs can be linked to large curvature perturbations generated during inflation. When these perturbations exceed a critical threshold, they can collapse gravitationally to form PBHs upon horizon reentry. PBHs are formed when local density contrast surpass a threshold value δ_c , with $\frac{\delta\rho}{\rho} \gtrsim \delta_c \sim 1$, indicating gravitational collapse. Various mechanisms have been proposed to generate such fluctuations, including quantum fluctuations during single-field [10–14] and multi-field [15–18] inflation, collapse of cosmic string loops [19–23], domain wall collapse [24, 25], and bubble collisions during phase transitions [26], and some more fancy mechanisms [27–32]. While the exact formation mechanism for PBHs remain a topic of further investigation, an alternative, observation-driven, route to study PBH evolution is to perform a model-independent analysis and to investigate how the parameters can be constrained by future interferometry missions.

While the standard reheating scenario assumes that the inflaton field decays into radiation, thereby initiating the radiation-dominated era [33–42], the PBH reheating scenario presents an alternative, and interesting, possibility. In this framework, PBHs form during a non-standard cosmological epoch characterized by a background equation of state parameter w_ϕ different from radiation. Depending on the properties of the inflaton potential and the dynamics of the post-inflationary era, the value of w_ϕ can range between 0 (matter-like domination) and 1 (stiff fluid domination). In this scenario, due to their non-relativistic nature, PBHs behave like pressureless matter and can dominate the Universe’s energy density before evaporating via Hawking radiation. This evaporation process injects energy into the cosmic plasma, triggering the reheating of the Universe and marking the onset of the radiation-dominated era [43–54]. Such a scenario naturally connects the properties of PBHs to the dynamics of the reheating epoch, offering a novel observational window into the post-inflationary Universe.

A remarkable feature of the PBH reheating scenario is the generation of stochastic GW backgrounds. Two distinct mechanisms contribute to the production of GWs in this context. First, the inhomogeneous spatial distribution of PBHs induces isocurvature density perturbations, which act as secondary sources of GWs during the PBH-dominated era [55–65]. These induced GWs originate from the Poissonian nature of the PBH number density fluctuations. Second, the sudden transition from PBH domination to radiation domination, driven by PBH evaporation, amplifies adiabatic curvature perturbations and

generates an additional GW signal [61, 62, 64–68]. The spectrum of these GWs carries distinctive features that encode information about the PBH parameters, the background equation of state, and the duration of the PBH-dominated era.

The detection of these GW spectra would offer a unique probe of the PBH reheating scenario and the associated non-standard cosmological dynamics [69]. Future interferometry missions, such as the Laser Interferometer Space Antenna (LISA) [70, 71] and the Einstein Telescope (ET) [72, 73], are particularly well-suited to detect the GW spectra associated with PBH reheating. LISA, operating in the millihertz frequency range, is sensitive to GWs generated by heavier PBHs with masses around $(10^5\text{--}10^8)$ g, while ET, probing higher frequencies, can detect the spectra from lighter PBHs with masses around $(1\text{--}10^7)$ g. The complementary sensitivity ranges of these missions provide a unique opportunity to explore a wide range of PBH masses and the associated reheating dynamics.

In this work, we systematically investigate the GW signatures of PBH reheating and their detection prospects in future GW observatories. We outline the theoretical framework for PBH formation during non-standard reheating, the associated GW production mechanisms, and the expected spectral features. Our analysis employs a combination of signal-to-noise ratio calculations, Fisher forecast analysis, and Markov chain Monte Carlo (MCMC) analysis using mock data, leading to a quantitative estimation of the prospects of detecting these spectra. By linking the GWs amplitude and frequency to the PBH parameters — such as the formation mass, energy fraction and the background equation of state — we demonstrate how future GW observations can shed light on the physics of PBH reheating and the early Universe’s non-standard evolution.

This paper is organized as follows: In Section 2, we provide a brief overview of the primordial black hole reheating scenario. Section 3 outlines the detection prospects of the GW spectra in future interferometry missions. Section 4 discusses the production of GW from PBH reheating, focusing on two distinct sources: isocurvature-induced GWs and adiabatic-induced GWs. We present the detection prospects and estimations for uncertainties associated with PBH and background parameters for both LISA and ET. In Section 5, we present a combined analysis of both GW sources, highlighting the complementary roles of LISA and ET in exploring the PBH reheating parameters. Finally, Section 6 summarizes our findings and discusses the implications of future GW observations in probing the non-standard cosmological epoch associated with PBH reheating.

2 Brief overview of the primordial black hole reheating

After inflation ends, the inflaton field oscillates around the minimum of its potential. Depending on the shape of the potential at the minima, the equation of state (EoS) w_ϕ of the scalar field can differ from that of radiation ($w_\phi = 1/3$), and the duration of reheating depends on how quickly the inflaton decays into standard model particles. In the standard reheating scenario, the Universe enters the radiation-dominated (RD) era as the oscillating inflaton field decays, with its energy dominating the Universe before it decays [34–39].

However, in the scenario we are considering a different background evolution, where PBHs form during the inflaton-dominated phase. We consider this as a formation in some non-standard phase with w_ϕ . Important to note that, after formation, PBHs evolve like non-relativistic matter, causing their energy density to dilute more slowly than the total

energy density, since the effective EoS satisfies $0 < w_\phi \leq 1$ ¹. As a result, PBHs could dominate the Universe before decaying, provided their initial abundance is large enough [43–46, 52]. We thus envision a PBH-dominated era sandwiched between the w_ϕ dominated phase and the standard radiation-dominated era.

The evolution of the PBHs is typically described by two key quantities: the formation mass (M_{in}) and the energy fraction (β), which represent the portion of the total energy density that goes into creating PBHs. Assuming ultralight PBHs form during the post-inflationary era in a background of w_ϕ , the Boltzmann equations for the various energy components can be written as:

$$\frac{d\rho_\phi}{da} + 3(1 + w_\phi)\frac{\rho_\phi}{a} = -\frac{\Gamma_\phi\rho_\phi(1 + w_\phi)}{aH}, \quad (2.1)$$

$$\frac{d\rho_r}{da} + 4\frac{\rho_r}{a} = -\frac{\rho_{\text{BH}}}{M_{\text{BH}}}\frac{dM_{\text{BH}}}{da} + \frac{\Gamma_\phi\rho_\phi(1 + w_\phi)}{aH} \simeq -\frac{\rho_{\text{BH}}}{M_{\text{BH}}}\frac{dM_{\text{BH}}}{da}, \quad (2.2)$$

$$\frac{d\rho_{\text{BH}}}{da} + 3\frac{\rho_{\text{BH}}}{a} = \frac{\rho_{\text{BH}}}{M_{\text{BH}}}\frac{dM_{\text{BH}}}{da}, \quad (2.3)$$

$$\frac{dM_{\text{BH}}}{da} = -\epsilon\frac{M_{\text{p}}^4}{M_{\text{BH}}^2}\frac{1}{aH}. \quad (2.4)$$

Here, $\epsilon \equiv 3.8\left(\frac{\pi}{480}\right)g_*(T_{\text{BH}})$, and $g_*(T_{\text{BH}})$ represents the number of relativistic degrees of freedom. The factor 3.8 accounts for the greybody factor [75–77]. ρ_ϕ, ρ_r and ρ_{BH} represent the energy densities of inflaton, radiation and PBHs, respectively. Note that in the change of the inflaton energy density, we neglect the decay term compared to the Universe’s expansion ($\Gamma_\phi \ll H$), assuming that lifetime of the inflaton is much longer than the timescale required for the Universe to reach PBH-domination. As a result, the dominant source of radiation energy density will be the evaporation of PBHs. The change in the PBH energy density is influenced by two processes: Hawking evaporation and dilution due to cosmic expansion. The mass of a PBH at any time can be determined by solving Eq. (2.4) as

$$M_{\text{BH}} = M_{\text{in}}(1 - \Gamma_{\text{BH}}(t - t_{\text{in}}))^{1/3}, \quad (2.5)$$

where $\Gamma_{\text{BH}} = \frac{3\epsilon M_{\text{p}}^4}{M_{\text{in}}^3}$, and t_{in} and a_{in} are the formation time of the PBH and the scale factor associated with the formation, respectively. The lifetime of a PBH is given by $t_{\text{ev}} = 1/\Gamma_{\text{BH}}$. We assume that PBHs form during a w_ϕ dominated phase due to the gravitational collapse of density fluctuations. Therefore, the formation mass of the PBHs (M_{in}) can be expressed as:

$$M_{\text{in}} = \gamma\frac{4}{3}\pi\frac{\rho_\phi(a_{\text{in}})}{H_{\text{in}}^3} = \frac{4\pi\gamma M_{\text{p}}^2}{H_{\text{in}}}, \quad (2.6)$$

where $\gamma \equiv w_\phi^{3/2}$ is the collapse efficiency [2]². In Fig. 1, we illustrate the evolution of various energy components as a function of the normalized scale factor a/a_{in} . From the

¹We exclude exact matter domination ($w_\phi = 0$) because PBH formation in an early matter-dominated phase would take much longer to form an apparent horizon [74] and preventing PBHs from becoming dominant, what we assume here.

²At this point, it is worth mentioning that a more precise method exists for estimating the formation mass of PBHs, which is sensitive to both the w_ϕ of the cosmological background fluid and the profile of the scalar fluctuations [74, 78–84]. However, a comprehensive analytical study to fully understand the values of γ in the context of PBH formation during post-inflationary era has yet to be conducted. Therefore, we have opted to use the analytical relation for collapse efficiency as suggested by Carr and Hawking.

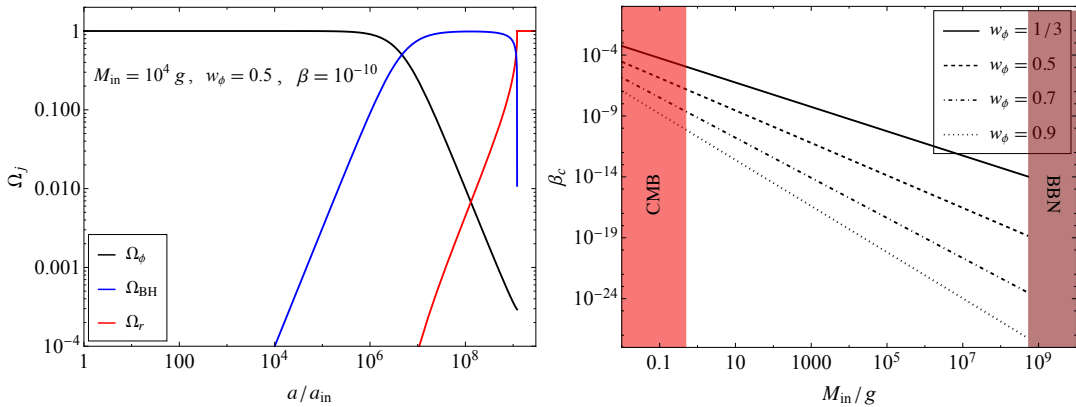


Figure 1: Left panel: The evolution of the normalized energy densities, $\Omega_j = \rho_j/3M_{\text{p}}^2H^2$, as a function of the scale factor is shown. This figure illustrates the PBH reheating scenario, where PBH evaporation completes after it has dominated the entire background. **Right panel:** β_c as a function of M_{in} for various values of w_ϕ , with shaded regions indicating the excluded ranges: the red region represents the CMB constraint on the formation mass of PBHs, and the brown region corresponds to the BBN constraint.

figure, it is evident that there exists a critical value of β , denoted β_c , above which the PBH energy density exceeds the inflaton energy density before the PBHs evaporate, with reheating occurring primarily through PBH evaporation. We refer to this scenario as PBH reheating. Consequently, β_c turns out to be

$$\beta_c = \left[\frac{\epsilon}{2\pi(1+w_\phi)\gamma} \frac{M_{\text{p}}^2}{M_{\text{in}}^2} \right]^{\frac{2w_\phi}{1+w_\phi}} \simeq \left(\frac{2.8 \times 10^{-6}}{w_\phi^{3/4} \sqrt{1+w_\phi}} \right)^{\frac{4w_\phi}{1+w_\phi}} \left(\frac{1 \text{ g}}{M_{\text{in}}} \right)^{\frac{4w_\phi}{1+w_\phi}}. \quad (2.7)$$

It can be found from the above Eq. (2.7) that $\beta_c \simeq 5.6 \times 10^{-6} \left(\frac{1 \text{ g}}{M_{\text{in}}} \right)$ for $w_\phi = 1/3$, and $\beta_c \simeq 6.1 \times 10^{-8} \left(\frac{1 \text{ g}}{M_{\text{in}}} \right)^{\frac{4}{3}}$ for $w_\phi = 1/2$. In the right panel of Fig. 1, how the critical parameter β_c varies with the background EoS is depicted. The figure clearly illustrates that PBH-domination becomes easier, as the value of w_ϕ increases, resulting in a shift of β_c to lower values.

The end of the evaporation marks the point of reheating, and the radiation temperature corresponding to this evaporation point is given by: ³

$$T_{\text{ev}} = \left(\frac{360\epsilon^2}{\pi^2 g_*(T_{\text{ev}})} \right)^{1/4} \left(\frac{M_{\text{p}}}{M_{\text{in}}} \right)^{3/2} M_{\text{p}} = 2.7 \times 10^{10} \left(\frac{1 \text{ g}}{M_{\text{in}}} \right)^{3/2}, \quad (2.8)$$

where we assume $g_*(T_{\text{ev}}) = 106.75$ and $g_*(T_{\text{BH}}) = 108$. To ensure successful Big Bang Nucleosynthesis (BBN), the Universe must be radiation-dominated during BBN. This requires all PBHs to evaporate before BBN, *i.e.*, $T_{\text{ev}} \geq T_{\text{BBN}} = 4 \text{ MeV}$ [86–88]. This sets an

³Note that for $\beta < \beta_c$, unlike the case where PBHs dominate the background before they evaporate, PBHs are formed and evaporate during the inflaton-dominated phase, without ever becoming the dominant energy component of the Universe. In this scenario, reheating through PBH evaporation can only occur if the inflaton’s equation of state corresponds to a stiff fluid, *i.e.*, $w_\phi > 1/3$, and the production rate due to inflaton decay or scattering remains subdominant, such that $\Gamma_\phi \rho_\phi (1+w_\phi) < -\frac{\rho_{\text{BH}}}{M_{\text{BH}}} \frac{dM_{\text{BH}}}{dt}$ (for more details, see Ref. [52, 85]). We exclude this type of PBH reheating scenario throughout our analysis.

upper limit on M_{in} as determined by Eq. (2.8). On the other hand, data from Planck-2018, along with BICEP2/*Keck* [89, 90], provides an upper bound on the tensor-to-scalar ratio ($r_{0.05} < 0.036$), which in turn constrains the Hubble parameter during inflation, assuming de Sitter like inflation. This constraint is given by $H_{\text{inf}} < 4.8 \times 10^{13}$ GeV, providing a lower bound on M_{in} according to Eq. (2.6). Therefore, from both BBN and cosmic microwave background (CMB) observations, one can obtain an upper and lower bound on M_{in} , respectively, given by:

$$0.5 \text{ g} \left(\frac{\gamma}{0.2} \right) \lesssim M_{\text{in}} \lesssim 4.8 \times 10^8 \text{ g} \left(\frac{g_*(T_{\text{ev}})}{106.75} \right)^{-1/6} \left(\frac{g_*(T_{\text{BH}})}{108} \right). \quad (2.9)$$

Ultralight PBHs can contribute to the generation of GWs in several ways. For instance, large curvature perturbations which is associated with the PBH formation can induce GWs [91–98], stochastic GW background can be generated by gravitons produced from the evaporation of PBHs [99], induced GWs through fluctuations in the PBH number density, which are isocurvature in nature [55, 56, 59, 61–65, 100, 101]. Additionally, the sharp transition from matter-domination (PBH-domination) to radiation-domination, driven by PBH evaporation, enhances induced GWs, which are adiabatic primordial curvature perturbations [61, 62, 66, 102]. Since ultralight PBHs form near the end of inflation, the secondary GWs induced by scalar perturbations from PBH formation typically occur at very high frequencies, close to the wave number associated with end of inflation. The stochastic GW background resulting from PBH evaporation into gravitons also contributes to high-frequency GWs. Thus, we focus on two relevant sources within the detectable range: one related to induced GWs from isocurvature perturbations arising from PBH density fluctuations, and the other from adiabatic fluctuations, which become significant due to the sudden transition from PBH domination to radiation domination. Our ultimate goal is to link the amplitude and frequency dependency of these GWs to PBH and background parameters ($w_\phi, \beta, M_{\text{in}}$), so that any future detection of stochastic GW background can provide insights into both the early PBH domination and the phase preceding it.

3 Steps to investigate detection prospects in interferometry missions

Before discussing specific GW sources and their detectability with future GWs missions like ET and LISA, let us first discuss very briefly the steps we have followed in investigating the detection prospects of such signals in interferometry missions, in order to make the present article self-content from the point of view of the potential readers.

3.1 Signal-to-noise ratio for different detectors

Noise plays a key role in any observational data, so evaluating the signal-to-noise ratio (SNR) is essential for determining the detectable prospects of the signal. SNR for the GW missions can be calculated as [103, 104]

$$\text{SNR} \equiv \sqrt{\tau_{\text{obs}} \int_{f_{\text{min}}}^{f_{\text{max}}} df \left(\frac{\Omega_{\text{GW}}(f, \{\theta\}) h^2}{\Omega_{\text{GW}}^{\text{noise}}(f) h^2} \right)^2}, \quad (3.1)$$

where $\Omega_{\text{GW}}(f, \{\theta\}) h^2$ represents the GW energy density predicted by a specific theory, with $\{\theta\} (\equiv w_\phi, \beta, M_{\text{in}}$ in our case) being the model parameters. $\Omega_{\text{GW}}^{\text{noise}}(f) h^2$ contains noise

characteristic of the detector, operating within the frequency-range between $[f_{\min}, f_{\max}]$ and τ_{obs} denotes the duration of observation. In this analysis, we have considered ET and LISA as the representative missions, for which the noise spectra for instrumental noise are described in App. A. In Table-1, the frequency-range and observation time for the detectors are presented. For both detectors, we have set the observational threshold for the SNR to be 1.

<i>Detectors</i>	<i>Frequency range</i>	τ_{obs}
LISA	$[10^{-4} - 1]$ Hz	4 years
ET	$[1 - 10^4]$ Hz	5 years

Table 1: *Specification of the detectors under consideration.*

3.2 Statistical analysis with likelihood function

A common approach in this context is to divide the frequency range of GW detectors into logarithmically spaced bins of equal weight [105], ensuring that each bin contains a well-defined contribution to the overall signal. In each bins, there exist

$$n_b \equiv [(f_b - f_{b-1})\tau_{\text{obs}}], \quad (3.2)$$

with $b \in [0, N_b]$. We have set $N_b = 100$ in our analysis for all the detectors⁴. The square brackets represent integer value of n_b . The Gaussian distribution of Likelihood function for $\Omega_{\text{sig}}(f_b, \{\theta\})$ [106] can be expressed as

$$\mathcal{L}(\theta) = \prod_{b=1}^{N_b} \sqrt{\frac{n_b}{2\pi\Omega_n(f_b)^2}} \exp\left(-\frac{n_b(\Omega_{\text{sig}}(f_b, \{\theta\}) - \Omega(f_b))^2}{\Omega_n(f_b)^2}\right). \quad (3.3)$$

where $\Omega_{\text{fid}}(f_b) \equiv \Omega_{\text{sig}}(f_b, \{\theta_{\text{fid}}\})$ with $\{\theta_{\text{fid}}\}$ indicates the fiducial values of the model parameters. Instead of directly maximizing the likelihood (\mathcal{L}), a more convenient approach is to maximize its logarithm, which can be defined as

$$\mathcal{L}(\theta) \equiv \ln(\mathcal{L}(\theta)). \quad (3.4)$$

It is generally called the log-likelihood function or χ^2 -distribution.

Fisher forecast analysis:

Although SNR analysis assesses the parameter space where the detection is robust, it does not provide precise measurements of the parameters being probed. Fisher matrix analysis estimates the uncertainties associated with the parameter, offering insight into the precision of the parameter during measurement. The Fisher matrix can be expressed, in terms of the log-likelihood, as [106]

$$F_{ij} = \left\langle -\frac{\partial^2 \mathcal{L}(\theta)}{\partial \theta_i \partial \theta_j} \right\rangle, \quad (3.5)$$

⁴ $N_b = \mathcal{O}(100)$ ensures the Gaussian approximation [105].

where angular brackets indicate the ensemble average over observational data *i.e.*, the data that would be collected if the true Universe were described by the given model, around which the derivative is evaluated. Under the Gaussian approximation, the Fisher matrix can be expressed as [106]

$$F_{ij} = \tau_{\text{obs}} \sum_{b=1}^{N_b} \frac{2\Delta f_b}{\Omega_n^2} \frac{\partial \Omega_{\text{sig}}}{\partial \theta_i} \frac{\partial \Omega_{\text{sig}}}{\partial \theta_j}, \quad (3.6)$$

where Δf_b is the frequency binning, defined as $f_b - f_{b-1}$. The reciprocal of the Fisher matrix, $[C_{ij}] \equiv [F_{ij}]^{-1}$, provides the covariance matrix, in which the square roots of the diagonal elements (C_{ii}) exhibit the uncertainties associated with the model parameters (θ_i).

Markov chain Monte Carlo analysis:

As discussed in the previous section, the Fisher matrix provides insights only into the uncertainties for a given fiducial value. To obtain a more comprehensive inference of the parameters, we perform a rigorous MCMC analysis for the GW detectors ET and LISA. In this context, we employ the same likelihood function as in Eq. (3.3), but instead of $\Omega_{\text{fid}}(f_b)$, we utilize mock data. To generate the mock catalogues, we have chosen a set of parameters such that *i)* SNR > 1 and *ii)* relative uncertainties on the parameters (obtained from Fisher analysis) less than 1 *i.e.* $\Delta\theta/\theta < 1$. To make it more realistic, we have sampled the chosen set of parameters from a normal distribution, incorporating the noise spectra associated with the detectors [107], ensuring that the mock catalogue is different depending on the spectra and the detectors. The desired posterior distributions of the parameters are expressed as the product of likelihood and priors on the parameters. The prior ranges are tabulated in Table-2. To perform the whole analysis, we have used the publicly available sampler code `emcee` [108], whereas `GetDist` [109] is used to plot the posterior distribution.

<i>Parameter</i>	<i>Prior</i>
w_ϕ	Flat, 0.1 \rightarrow 0.99
$\log_{10}(\beta)$	Flat, -22 \rightarrow 0
$\log_{10}(M_{\text{in}}/1 \text{ g})$	Flat, -0.3 \rightarrow 8.62

Table 2: Priors on the all three parameters for ET and LISA.

4 Gravitational waves from PBH reheating

As mentioned earlier, two promising sources of gravitational waves are expected to arise in the PBH reheating scenario: one associated with isocurvature fluctuations and the other with adiabatic fluctuations. In this section, we will focus on each of these sources individually and investigate the detection prospects and possible constraints on the associated PBH parameters. We will make use of the statistical techniques as discussed in the previous section, for the two upcoming interferometer missions, namely, LISA and ET, and evaluate their potential detection prospects of the PBH parameters.

The observed quantity, GW spectral energy density, can be defined, in terms of oscillation averaged tensor power spectrum ($\overline{\mathcal{P}_h}$), as

$$\Omega_{\text{GW}}(k, \eta) = \frac{k^2}{12\mathcal{H}^2} \overline{\mathcal{P}_h(k, \eta)}. \quad (4.1)$$

Here, \mathcal{H} is the Hubble parameter defined in terms of the conformal time (η), *i.e.*, $\mathcal{H} \equiv \frac{da}{d\eta} \frac{1}{a}$. This spectra is calculated at the conformal time during the RD epoch when GWs are well inside the horizon and propagate freely. Hence, at the present time, GW spectra can be calculated as [110]

$$\Omega_{\text{GW}}^{(0)}(k) h^2 \simeq c_g \Omega_{\text{r}}^{(0)} h^2 \Omega_{\text{GW}}(k, \eta) \simeq 1.62 \times 10^{-5} \Omega_{\text{GW}}(k, \eta). \quad (4.2)$$

The parameter c_g is given by $c_g \equiv \left(\frac{g_{*k}}{g_{*0}}\right) \left(\frac{g_{*s0}}{g_{*sk}}\right)^{4/3}$, where (g_{*k}, g_{*sk}) and (g_{*0}, g_{*s0}) denote the effective number of relativistic degrees of freedom associated with the energy density of radiation and entropy, respectively, at the time when the wave number k re-enters the Hubble radius and at the present epoch. Additionally, $\Omega_{\text{r}}^{(0)} h^2 \simeq 4.18 \times 10^{-5}$ represents the radiation energy density today. Now $\overline{\mathcal{P}_h(k, \eta)}$ can be expressed, in terms of curvature power spectrum (\mathcal{P}_Φ), as [111]

$$\overline{\mathcal{P}_h(k, \eta)} = 8 \int_0^\infty dv \int_{|1-v|}^{1+v} du \left(\frac{(1+v^2-u^2)^2 - 4v^2}{4uv} \right)^2 \mathcal{P}_\Phi(uk) \mathcal{P}_\Phi(vk) \overline{I^2}(x, u, v), \quad (4.3)$$

with $x \equiv k\eta$. The kernel function, $I(x, u, v)$ carries the complete information of time-evolution in \mathcal{P}_h . Now due to the sudden transition from PBH-domination to RD, the contribution, coming right after the end of PBH-domination, is the dominant one [112]. Thus, \mathcal{P}_Φ can be estimated at the end of PBH-domination. We now present the form of the gravitational wave spectrum for two different sources after solving the momentum integral in u and v , along with their detection prospects in light of upcoming interferometry missions.

4.1 Gravitational waves induced by isocurvature fluctuations

For $\beta > \beta_c$, PBHs indirectly serve as a significant source of induced gravitational waves. The initial inhomogeneous distribution of PBHs creates isocurvature fluctuations, which, by the time PBHs dominate, transform into adiabatic perturbations. It can be assumed that the PBH-distribution to be a Poisson spectrum for the density fluctuation and we define the initial isocurvature perturbation as $\frac{\delta\rho_{\text{BH}}(\mathbf{x})}{\rho_{\text{BH}}} \equiv S_i(\mathbf{x})$. If d be the mean separation between the PBHs, the two-point correlation for S_i in the real-space, can be expressed as [113]

$$\left\langle \frac{\delta\rho_{\text{BH}}(\mathbf{x})}{\rho_{\text{BH}}} \frac{\delta\rho_{\text{BH}}(\tilde{\mathbf{x}})}{\rho_{\text{BH}}} \right\rangle = \frac{4\pi}{3} \left(\frac{d}{a}\right)^3 \delta(\mathbf{x} - \tilde{\mathbf{x}}). \quad (4.4)$$

In Fourier space this correlation has the following form [113, 114]

$$\left\langle S_i(k) S_i(\tilde{k}) \right\rangle = \frac{2\pi^2}{k^3} \mathcal{P}_{\text{BH},i}(k) \delta(k + \tilde{k}), \quad (4.5)$$

where the initial power spectra ($\mathcal{P}_{\text{BH},i}(k)$) can be defined as

$$\mathcal{P}_{\text{BH},i}(k) \equiv \frac{k^3}{2\pi} \frac{4\pi}{3} \left(\frac{d}{a}\right)^3 = \frac{2}{3\pi} \left(\frac{k}{k_{\text{UV}}}\right)^3. \quad (4.6)$$

Hence, the initial power spectrum is directly related with the ultraviolet (UV) cutoff scale (k_{UV}) which can be expressed as [114]

$$k_{\text{UV}} \simeq 1.1 \times 10^4 \text{ Hz} \left(\frac{g_{*,s}(T_{\text{ev}})}{106.75} \right)^{-1/3} \left(\frac{g_*(T_{\text{ev}})}{106.75} \right)^{1/4} \left(\frac{g_*(T_{\text{BH}})}{108} \right)^{1/6} \left(\frac{M_{\text{in}}}{10^4 \text{ g}} \right)^{-5/6}. \quad (4.7)$$

The evolution of the Newtonian potential (Φ), can be related with initial isocurvature perturbation as

$$\Phi'' + 3\mathcal{H}(1 + c_s^2)\Phi' + ((1 + 3c_s^2)\mathcal{H}^2 + 2\mathcal{H}' + c_s^2 k^2)\Phi = \frac{1}{2}a^2 c_s^2 \rho_{\text{BH}} S_i, \quad (4.8)$$

with c_s representing the sound speed. The prime ($'$) in the expression indicates the derivative with respect to η . This isocurvature perturbation acts as a source term in the tensor power spectrum $\mathcal{P}_h(k)$, ultimately inducing second-order GWs. The spectral energy density of these GWs, particularly near the resonant peak, is given by [115]:

$$\Omega_{\text{GW,res}}(k) \approx \Omega_{\text{GW,res}}^{\text{peak}} \left(\frac{k}{k_{\text{UV}}} \right)^{11/3} \Theta_{\text{UV}}^{(\text{iso})}(k), \quad (4.9)$$

where the amplitude near the peak can be expressed as

$$\Omega_{\text{GW,res}}^{\text{peak}} = C^4(w_\phi) \frac{c_s^{7/3} (c_s^2 - 1)^2}{576 \times 6^{1/3} \pi} \left(\frac{k_{\text{BH}}}{k_{\text{UV}}} \right)^8 \left(\frac{k_{\text{UV}}}{k_{\text{ev}}} \right)^{17/3}, \quad (4.10)$$

with $C(w_\phi) = \frac{9}{20} \alpha_{\text{fit}}^{-\frac{1}{3w_\phi}} \left(3 + \frac{1-3w_\phi}{1+3w_\phi} \right)^{-\frac{1}{3w_\phi}}$, considering $\alpha_{\text{fit}} \approx 0.135$. The PBH domination scale (k_{BH}) is defined as following

$$k_{\text{BH}} = \sqrt{2} \gamma^{1/3} \beta^{\frac{1+w_\phi}{6w_\phi}} k_{\text{UV}}. \quad (4.11)$$

The cutoff function, $\Theta_{\text{UV}}^{(\text{iso})}(k)$, is defined in App. B. The infrared (IR) region belongs to relatively lower frequencies where $k \ll k_{\text{UV}}$. The prime contribution to this regime can be expressed as [115]

$$\Omega_{\text{GW,IR}}(k) = C^4(w_\phi) \frac{c_s^4}{120\pi^2} \left(\frac{2}{3} \right)^{\frac{1}{3}} \left(\frac{k_{\text{BH}}}{k_{\text{UV}}} \right)^8 \left(\frac{k_{\text{UV}}}{k_{\text{ev}}} \right)^{\frac{14}{3}} \left(\frac{k}{k_{\text{UV}}} \right) \quad (4.12)$$

$$\simeq 9.03 \times 10^{24} C^4(w_\phi) \beta^{\frac{4(1+w_\phi)}{3w_\phi}} \left(\frac{\gamma}{0.2} \right)^{\frac{8}{3}} \left(\frac{M_{\text{in}}}{10^4 \text{ g}} \right)^{\frac{28}{9}} \left(\frac{k}{k_{\text{UV}}} \right). \quad (4.13)$$

In addition, a transition frequency f_{T} marks the boundary between the infrared (IR) tail of the GW spectrum and the region near the resonant peak [114]. This frequency is determined by equating the IR and resonant components of the GW spectrum: $\Omega_{\text{GW,IR}}(f_{\text{T}}) = \Omega_{\text{GW,res}}(f_{\text{T}})$. The transition frequency can be expressed as:

$$f_{\text{T}} = \frac{k_{\text{UV}}}{2\pi} \left[\left(10^{-6} \frac{M_{\text{in}}}{10^4 \text{ g}} \right)^{-2/3} \right]^{3/8}, \quad (4.14)$$

which depends solely on the PBH formation mass M_{in} . Thus, the complete isocurvature-induced GW spectrum is given by:

$$\Omega_{\text{GW,iso}}(f) = \begin{cases} \Omega_{\text{GW,res}}(f), & f \geq f_{\text{T}}, \\ \Omega_{\text{GW,IR}}(f), & f < f_{\text{T}}. \end{cases} \quad (4.15)$$

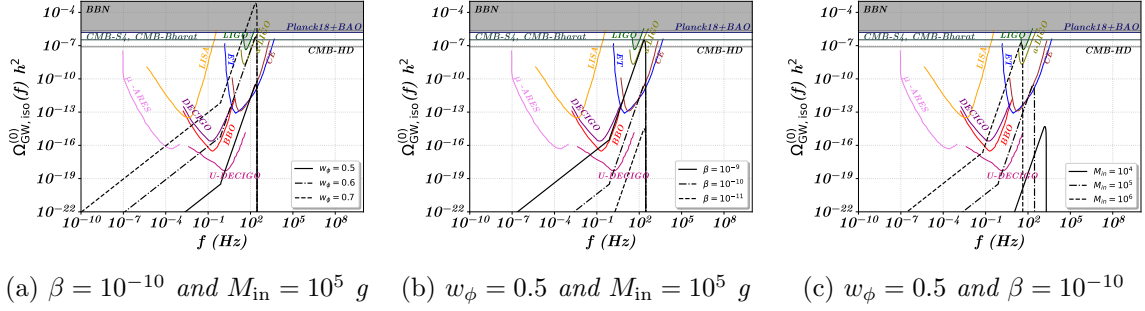


Figure 2: Induced gravitational wave spectrum at the present epoch due to *isocurvature fluctuations*. Each plot represents the variation of a single parameter while the other two are kept fixed.

Finally, the present-day isocurvature-induced GW spectrum, $\Omega_{\text{GW,iso}}^{(0)}(f) h^2$, can be obtained using Eq. (4.2).

In Fig. 2, we illustrate how each parameter affects the GW spectrum while keeping others fixed. The spectral slope near the peak, $\Omega_{\text{GW,res}} \propto k^{11/3}$ (i.e., Eq. (4.9)), remains independent of w_ϕ , with the peak frequency solely determined by M_{in} (i.e., the peak appear at the wave number k_{UV}). Lighter PBHs form and evaporate earlier, shifting GW peaks to higher frequencies (Fig. 2c). For a fixed M_{in} , the peak frequency remains unchanged, but its amplitude increases with w_ϕ (Fig. 2a) and β (Fig. 2b).

This behaviour can be explained using Eq. (4.10), as the background equation of state w_ϕ , where PBHs form, influences the GW amplitude through $C^4(w_\phi)$ and $\beta^{\frac{4(1+w_\phi)}{3w_\phi}}$. This β dependency arises from the ratio $(k_{\text{BH}}/k_{\text{UV}})^8$ in Eq. (4.10), making the amplitude highly sensitive to w_ϕ . The transfer function term, $C_4(w_\phi)$, enhances the GW amplitude for lower w_ϕ by reducing the gravitational potential decay, while $\beta^{\frac{4(1+w_\phi)}{3w_\phi}}$ has the opposite effect, increasing the amplitude for stiffer w_ϕ and suppressing it for softer w_ϕ . This can be easily understood from the fact that a stiffer equation of state ($w_\phi > 1/3$) prolongs the PBH-dominated phase, enhancing the GW signal, while a softer one ($w_\phi < 1/3$) shortens it, leading to suppression.

However, the isocurvature-induced peak alone cannot break the degeneracy between w_ϕ and β , as both influence the amplitude. To resolve this, we consider induced gravitational waves from inflationary adiabatic fluctuations, which we explore in the next section.

4.1.1 Statistical analysis in the light of the detectors

Fig. 2 shows that the GW spectra from the isocurvature source are well within the detection capabilities of ET and LISA. Therefore, we proceed with the statistical analysis of this source for the two detectors, as outlined in Sec. 3.

Evaluation of signal-to-noise ratio:

Fig. 3 and Fig. 5 depict the SNR in the w_ϕ - β plane for different values of M_{in} , corresponding to the future GW missions ET and LISA, respectively. The black solid line represents SNR = 1, while the regions where SNR > 1 are indicated by black arrows in both cases. Additionally, the region where $\beta < \beta_c$ and the constraints from GW overproduction—derived from the upper bound on ΔN_{eff} from BBN, with $\Delta N_{\text{eff}} = 0.28$ based on Planck legacy

data [116]—are highlighted in grey and light orange, respectively. In both scenarios, the SNR increases with β for a fixed w_ϕ and vice versa, a trend discussed in detail in the previous section.

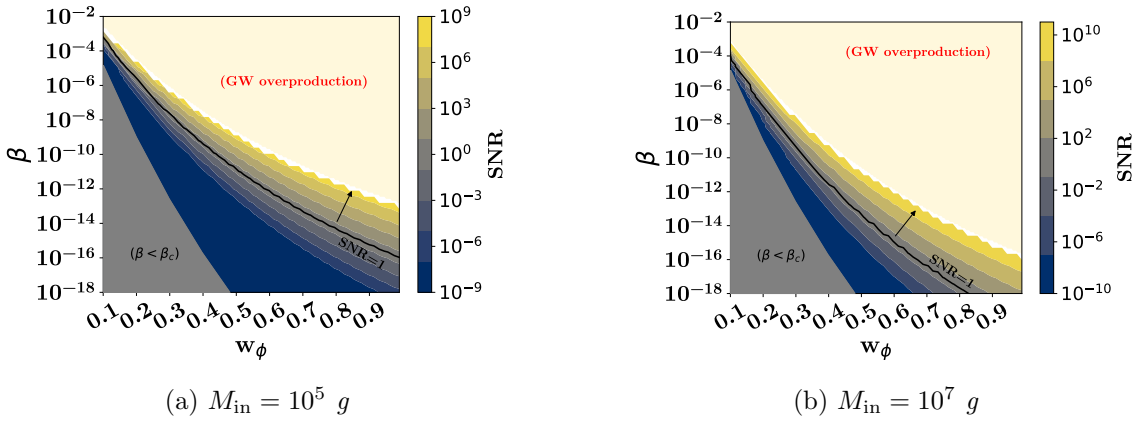


Figure 3: SNR plots for *ET* with two different values of M_{in} considering *isocurvature fluctuation*. The black solid line represents $\text{SNR} = 1$ with the arrow indicating the region $\text{SNR} > 1$. GW overproduction, derived from ΔN_{eff} limit at BBN, and $\beta < \beta_c$ are indicated by light orange and grey regions, respectively.

In Fig. 4, we show the range of parameters in order to achieve an $\text{SNR} > 1$ for the interferometry mission ET in the $w_\phi - \beta$ plane for different values of M_{in} . One interesting outcome of this analysis is that as the mass increases from a very low value, say 1 g, the region where $\text{SNR} > 1$ in the $w_\phi - \beta$ plane expands. However, after reaching an optimal value around 10^6 g , the region starts to shrink. Beyond $5 \times 10^7 \text{ g}$, no region in the $w_\phi - \beta$ plane remains where the SNR exceeds one. Such behaviour can be easily understood by comparing the peak frequency of the induced GW spectrum from the isocurvature source with the noise curve of the ET (see, for instance, Fig. 28 in the appendix). The peak frequency of this GWs spectrum is associated with k_{UV} and is given by: $f_{\text{peak}} \sim 1.7 \times 10^3 (M_{\text{in}}/10^4)^{-5/6} \text{ Hz}$. Since ET is most sensitive to frequencies in the range of approximately $1 - 4 \times 10^3 \text{ Hz}$, the peak frequency of the spectrum, which lies within the sensitivity for the mass range $10^3 - 10^7 \text{ g}$, determines the extent of the high-SNR region. Thus, any formation mass outside this range — either above or below — leads to a lower detection probability. This trend is also evident in Fig. 4, where for masses decreasing below 10^3 g , the parameter space shrinks, with the minimum mass providing $\text{SNR} > 1$ being around 1 g. Moreover, from the noise sensitivity curve, we see that the lowest value of $\Omega_{\text{GW}}^{\text{noise}} h^2$ occurs around 10 Hz, which corresponds to a formation mass of approximately 10^6 g . This aligns with our findings, as we observe the largest compatible parameter space in the $w_\phi - \beta$ plane around this mass scale.

On the other hand, for LISA, which is sensitive to frequencies in the range of $10^{-5} - 0.5 \text{ Hz}$, we find that only PBH masses above 10^8 g are compatible with its detection. However, the SNR values remain very close to 1, even for the maximum allowed PBH formation mass of $\sim 5 \times 10^8 \text{ g}$ (calculated by considering the evaporation point at the time of BBN), which is also clear from Fig. 5. This SNR-based analysis clearly indicates that, in terms of detection possibilities, the isocurvature source is more favourably detected by ET than LISA.

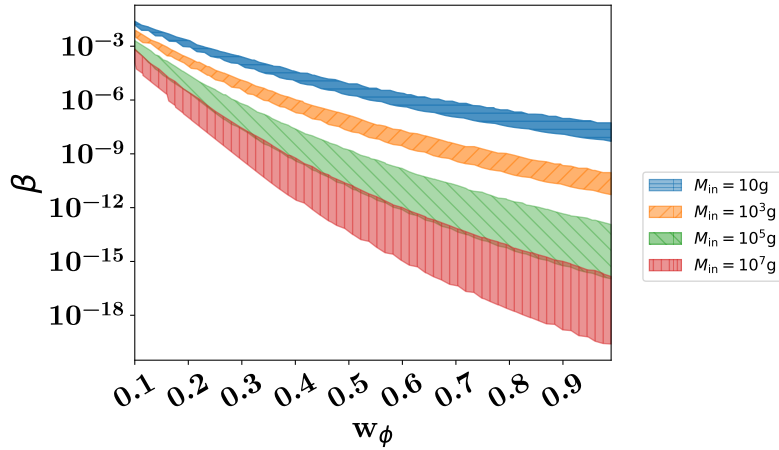


Figure 4: Illustration of extent of parameter space for various M_{in} where $\text{SNR} \geq 1$, considering *isocurvature induced GWs*, for ET. The upper limit comes from the GW overproduction, derived from ΔN_{eff} constraints at BBN.

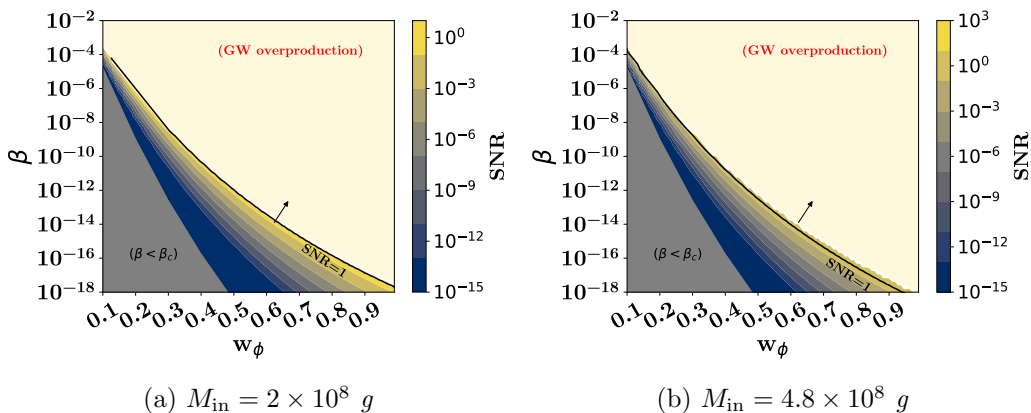


Figure 5: Illustration of SNR is same as Fig. 3, but for LISA.

Fisher forecast analysis:

As discussed earlier, the Fisher analysis provides insights into parameter uncertainties for a given source (see Sec. 3.2 for the analysis setup). Here, we use the Fisher forecast to estimate the uncertainties associated with the isocurvature fluctuation parameters, w_ϕ and β , for both ET and LISA. Note that in this analysis, we do not account for any uncertainties in the formation mass, M_{in} . Since Fisher forecast analysis depends on the choice of fiducial, we have chosen the fiducials from the range with $\text{SNR} \geq 1$ and outlined the range of parameters where the relative uncertainties associated with the parameters remain below 10^{-5} . One of the key findings of the Fisher analysis is that in most of the parameter space where $\text{SNR} > 1$, the relative uncertainties $\Delta w_\phi/w_\phi$ and $\Delta\beta/\beta$ are both large (*i.e.*, $\Delta w_\phi/w_\phi, \Delta\beta/\beta > 10$), as evident in Fig. 6 and Fig. 7. We find that only for masses around $M_{\text{in}} = 10^5 \text{ g}$, the $\text{SNR} > 1$ region is compatible with the uncertainty constraint $\Delta w_\phi/w_\phi < 10$, though $\Delta\beta/\beta$ remains greater than 10.

Thus, the Fisher analysis suggests that while ET has a high detection potential, provid-

⁵Typically, precise parameter estimation requires the relative uncertainties on the parameters to be less than 1. However, for isocurvature fluctuation, there is no region satisfying the condition $\Delta w_\phi/w_\phi (\Delta\beta/\beta) < 1$.

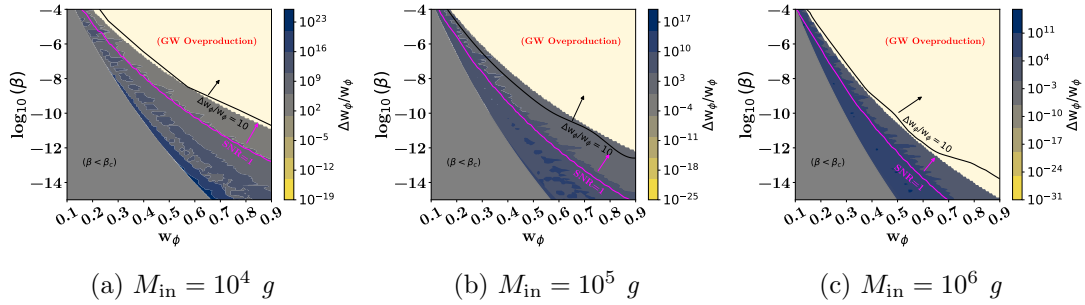


Figure 6: Illustration of relative uncertainties on w_ϕ , calculated by Fisher analysis, considering *isocurvature fluctuation*, for **ET**. Black (magenta) solid line indicates SNR = 1 ($\Delta w_\phi/w_\phi = 10$). The black (magenta) arrow indicates where SNR > 1 ($\Delta w_\phi/w_\phi < 10$).

ing high SNR values for isocurvature fluctuations, it is less effective in precisely constraining the associated parameters. On the other hand, for LISA, both the SNR and Fisher analyses indicate poor detection prospects, as shown in Fig. 8.

In summary, considering both SNR and Fisher analyses, we find that LISA has limited detection potential, while ET shows high SNR values but with large parameter uncertainties in most cases. This leads us to conclude that neither detector can convincingly achieve precise measurements of the parameters associated with isocurvature fluctuations, thus probing early physics considering such a source is difficult. Due to this limitation, in the next section, we explore another source of induced GWs, associated with adiabatic fluctuations originating from inflation.

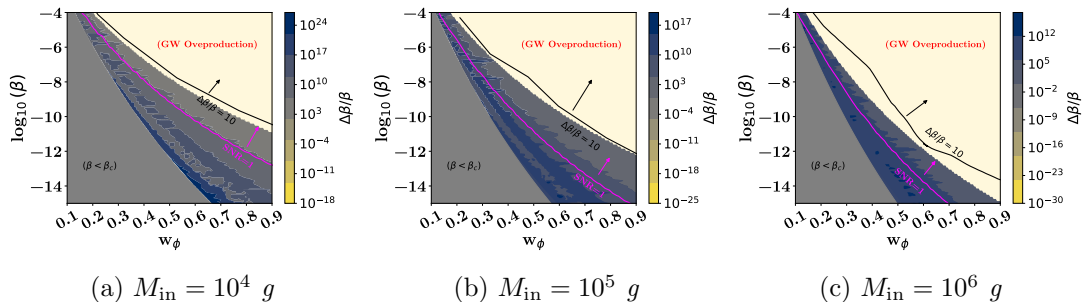


Figure 7: Representation is same as Fig. 6. However, it is the illustration of relative uncertainties on β , for **ET**.

4.2 Gravitational waves induced by adiabatic fluctuations

During the PBH-domination, the gravitational potential remains constant at the subhorizon scales. After PBH-domination, the gravitational potential oscillates due to radiation pressure in the RD era. During the transition to radiation domination, but before these oscillations begin, the potential on subhorizon scales decays, depending on the transition duration. Since PBH evaporation is nearly instantaneous, the transition is too short for significant decay before oscillations start. As a result, strong GWs are generated following the sudden PBH reheating scenario, even if the primordial curvature perturbation power spectrum remains nearly scale-invariant. We follow Ref. [114] for the analytic expressions, used in our study for this type of GW production. For the adiabatic initial conditions, \mathcal{P}_Φ

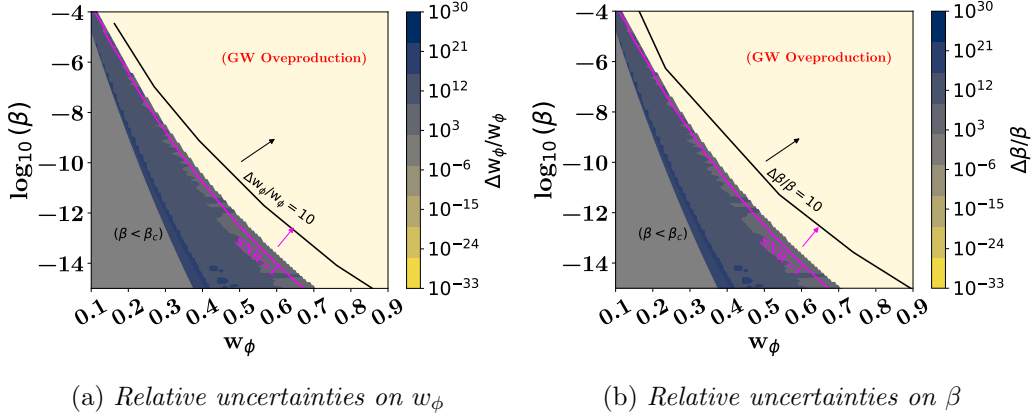


Figure 8: Illustration of relative uncertainties on w_ϕ and β , calculated by Fisher analysis, considering **isocurvature fluctuation**, for **LISA**. The analysis is performed for $M_{\text{in}} = 4.8 \times 10^8 g$. Rest is same as Fig. 6.

is related to the initial curvature power spectrum as

$$\mathcal{P}_{\Phi_0}(k) = A_s \left(\frac{k}{k_*} \right)^{n_s-1} \Theta(k_{\text{UV}} - k) \Theta(k - k_{\text{IR}}), \quad (4.16)$$

with k_{UV} and k_{IR} being the UV and IR cutoff scale, respectively. This changes the Eq. (4.3) as following:

$$\overline{\mathcal{P}_{h,\text{RD}}}(k, \eta, \bar{x} \gg 1) \propto \int_0^\infty dv \int_{|1-v|}^{1+v} du \left(4v^2 - (1 + v^2 - u^2)^2 \right)^2 (uv)^{n_{\text{eff}}(w_\phi)} \overline{\mathcal{I}_{\text{osc}}^2}(\bar{x}, u, v), \quad (4.17)$$

with $\bar{x} \equiv k\bar{\eta}$ and $\mathcal{I}_{\text{osc}}^2$ being the oscillatory kernel function, used to estimate the kernel function at the end of PBH-domination, as mentioned in Eq. (4.3). Here the effective spectral index (n_{eff}) is related to the scalar spectral index (n_s) by

$$n_{\text{eff}}(w_\phi) = -\frac{5}{3} + n_s + 2n(w_\phi). \quad (4.18)$$

For $k \ll k_{\text{BH}}$, $n(w_\phi) = 0$ whereas at the other regions, it is given by

$$n(w_\phi) \simeq \begin{cases} b/2 - 2 & w_\phi \lesssim 1/5 \\ -1.83 - 0.285b + 0.790b^2 & 1/5 < w_\phi < 2/3, \\ -(2 + b) & w_\phi \gtrsim 2/3 \end{cases}, \quad (4.19)$$

with $b \equiv (1 - 3w_\phi)/(1 + 3w_\phi)$.

For $k \gg k_{\text{BH}}$, we can also obtain the resonant contribution for the GW spectrum, which can be written as

$$\Omega_{\text{GW,res}}^{\text{ad}}(k) = \Omega_{\text{GW,res}}^{\text{ad,peak}} \left(\frac{k}{k_{\text{UV}}} \right)^{2n_{\text{eff}}(w_\phi)+7} \Theta_{\text{UV}}^{\text{(ad)}}(k), \quad (4.20)$$

where at $k = k_{\text{UV}}$, the amplitude is given by

$$\Omega_{\text{GW,res}}^{\text{ad,peak}} \simeq 9.72 \times 10^{32} \frac{3^{2n(w_\phi)+n_s}}{4^{3n(w_\phi)+n_s}} A_s^2 A_\Phi(w_\phi)^4 \gamma^{-4n(w_\phi)/3} \beta^{-\frac{2n(w_\phi)(w_\phi+1)}{3w_\phi}} \left(\frac{gH}{108} \right)^{-\frac{17}{9}} \left(\frac{M_{\text{in}}}{10^4 g} \right)^{\frac{34}{9}}. \quad (4.21)$$

The details of the cutoff function, $\Theta_{\text{UV}}^{(\text{ad})}(k)$, is discussed in App. B. At the proximity of k_{BH} and at $k \ll k_{\text{BH}}$, we can define the intermediate and IR part of the GW spectrum as follows:

$$\Omega_{\text{GW,mid}}^{\text{ad}}(k) = -\frac{A_s^2 A_\Phi(w_\phi)^4 c_s^4}{768(1+2n_{\text{eff}})} \left(\frac{3}{2}\right)^{\frac{2}{3}} \xi_1^{1+2n_{\text{eff}}} \left(\frac{k_{\text{BH}}}{k_{\text{UV}}}\right)^{2n_s-\frac{7}{3}} \left(\frac{k_{\text{UV}}}{k_{\text{ev}}}\right)^{\frac{14}{3}} \left(\frac{k}{k_{\text{UV}}}\right)^5, \quad (4.22)$$

$$\Omega_{\text{GW,IR}}^{\text{ad}}(k) = \frac{A_s^2 c_s^4 (3w_\phi + 5)^4}{10^4 (6n_s + 5)(w_\phi + 1)^4} \left(\frac{3}{2}\right)^{\frac{2}{3}} \left(\frac{\xi_2 k_{\text{BH}}}{k_{\text{UV}}}\right)^{\frac{5}{3}+2n_s} \left(\frac{k_{\text{UV}}}{k_{\text{ev}}}\right)^{\frac{14}{3}} \left(\frac{k}{k_{\text{UV}}}\right). \quad (4.23)$$

In the above expressions $A_\Phi(w_\phi)$ is given by

$$A_\Phi(w_\phi) = \begin{cases} \frac{2}{3b} (7.76 + 18.3b + 12.5b^2) & w_\phi < 1/5 \text{ or } w_\phi > 2/3 \\ 15.6 + 39.2b + 21.3b^2 & 1/5 < w_\phi < 2/3 \end{cases}. \quad (4.24)$$

Here, both ξ_1 and ξ_2 are the functions of w_ϕ . We have set $\xi_1 = 1$ throughout our analysis as it is a $\mathcal{O}(1)$ factor [114]. ξ_2 can be determined as follows:

$$\xi_2 = \begin{cases} \left(\frac{7.76+18.3b+12.5b^2}{(3w_\phi+5)/(5w_\phi+5)}\right)^{(1+3w_\phi)/(3+3w_\phi)} & w_\phi > 1/3 \\ \left(\frac{7.76+18.3b+12.5b^2}{(3w_\phi+5)/(5w_\phi+5)}\right)^{(2+6w_\phi)/(3+15w_\phi)} & w_\phi < 1/3 \end{cases}. \quad (4.25)$$

Now, the complete spectrum for the adiabatic contribution of the GW spectra ($\Omega_{\text{GW,ad}}(k)$), is simply the sum of the three parts. At the present epoch, the adiabatic contribution of the GW spectra ($\Omega_{\text{GW,ad}}^{(0)}(f)h^2$) can be estimated using Eq. (4.2).

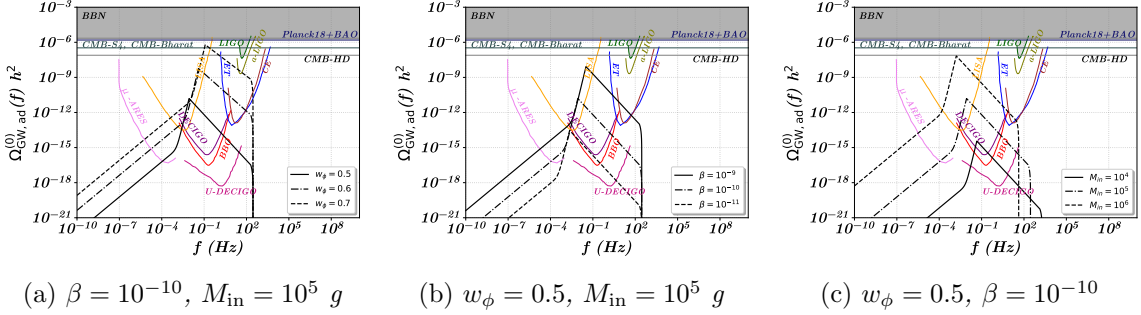


Figure 9: Induced gravitational wave spectrum at the present epoch due to **adiabatic fluctuation**. Each plot represents the variation of a single parameter while the other two are kept fixed.

Fig. 9 illustrates the impact of each of the three parameters on the GWs spectrum while keeping the others fixed, similar to our analysis for isocurvature fluctuations. Compared to the isocurvature case, the resonant part of the spectrum is broader and shifted to lower frequencies, as its peak is roughly associated with k_{BH} . In contrast, the isocurvature peak lies at k_{UV} , closer to the PBH formation wavenumber k_{in} . From Fig. 9, it is evident that increasing w_ϕ or β shifts the peak frequency to the right, *i.e.*, toward higher values. This can be understood as follows: a stiff EoS w_ϕ causes a greater redshift of the background relative to PBHs, which behave like dust. As a result, PBH-domination occurs earlier, pushing k_{BH} closer to the formation wave number k_{in} . Since the peak of the spectrum lies around k_{BH} , an increase in w_ϕ naturally leads to a shift in the peak frequency towards

higher frequency. A similar effect occurs for higher β , as a larger β facilitates earlier PBH-domination. Consequently, in both cases, the peak frequency shifts to higher values.

The behaviour of the GW spectra across different region (resonant part, intermediate part, IR part) can be understood using Eqs. (4.20), (4.22) and (4.23). At the resonant part of the GW spectra, the spectral dependence follows $k^{2n_{\text{eff}}(w_\phi)+7}$, where $n_{\text{eff}}(w_\phi)$ has a dependence on n_s , in contrast to the isocurvature fluctuation. For $n_s \lesssim 1$, the exponent ($2n_{\text{eff}}(w_\phi)+7$) becomes negative, explaining the negative slope of the GW spectrum at this region. Furthermore, GW spectra, at the intermediate and IR regimes, scales as k^5 and k , respectively. This transition is evident in Fig. 9, where the spectrum exhibits a sharp variation with f at the intermediate part, compared to IR part.

4.2.1 Statistical analysis in the light of the detectors

Similar to the isocurvature scenario, in this section, we proceed with the statistical analysis of the spectrum for ET and LISA, as they appear more promising for detecting the adiabatic spectrum, as evident from Fig. 9. LISA shows comparatively better prospects for detecting the adiabatic than the isocurvature source, at least based on what is observed in the Fig. 9.

Evaluation of signal-to-noise ratio:

Figs. 10 and 11 present the SNR plots for ET and LISA, respectively, for PBHs with masses of 10^5 g and 10^7 g. The plots follow the same structure as those for the isocurvature source. As in the isocurvature case, the SNR increases with β for a fixed w_ϕ and vice versa, as evident from Eq. (4.21). This trend arises because a higher β or w_ϕ extends the PBH-dominated era, thereby increasing the GW spectral density, which directly depends on the duration of PBH domination.

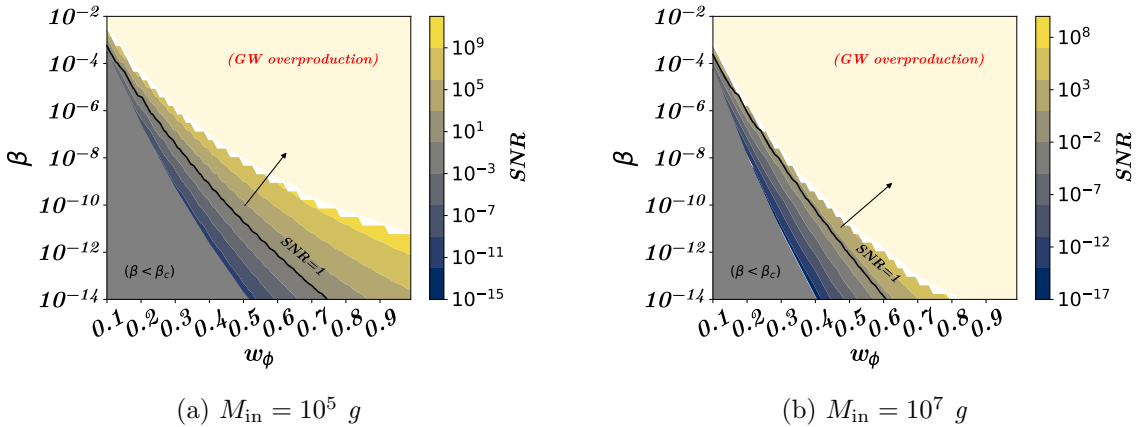


Figure 10: SNR plots for **ET** with two different values of M_{in} considering **adiabatic fluctuation**. Rest of the demonstration is same as Fig. 3.

The SNR analysis suggests that both ET and LISA show promise in detecting the adiabatic source, unlike the isocurvature one, which is only sensitive to ET. For ET (see, for instance, Fig. 12a), similar to the isocurvature source, we observe that the parameter span in the $w_\phi - \beta$ plane is considerably large for formation masses in the range $M_{\text{in}} \sim (10^3 - 10^7)$ g. However, it starts to shrink drastically for PBH masses above 10^7 g, with no available parameter space for high SNR > 1 for PBH masses above 4×10^7 g.

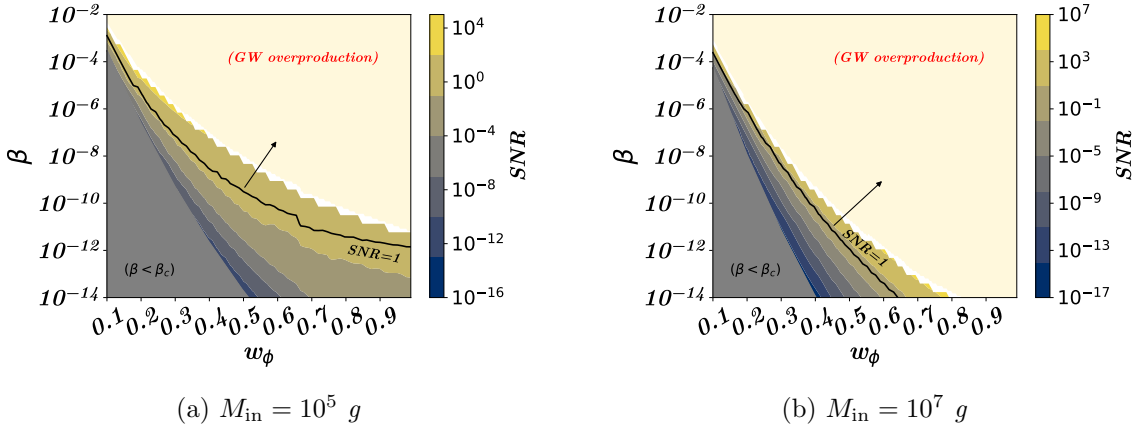


Figure 11: Figure is same as Fig. 3, but for *LISA*, considering *adiabatic fluctuation*.

On the other hand, for *LISA* (see, for instance, Fig. 12b), the parameter span starts from $M_{\text{in}} \sim 2 \times 10^4 \text{ g}$. For PBH masses below this threshold, the SNR remains < 1 for all possible ranges of w_ϕ and β . Furthermore, for *LISA*, the formation mass consistent with $\text{SNR} > 1$ lies in the range $M_{\text{in}} \sim (2 \times 10^4 - 5 \times 10^8) \text{ g}$, where the upper limit corresponds to the maximum mass value that evaporated just before BBN.

Thus, in terms of SNR, *LISA* is expected to be a promising mission for detecting induced GW spectra arising from adiabatic fluctuations, in contrast to the isocurvature scenario. However, for *ET*, we find that both sources are compatible with achieving high SNR values.

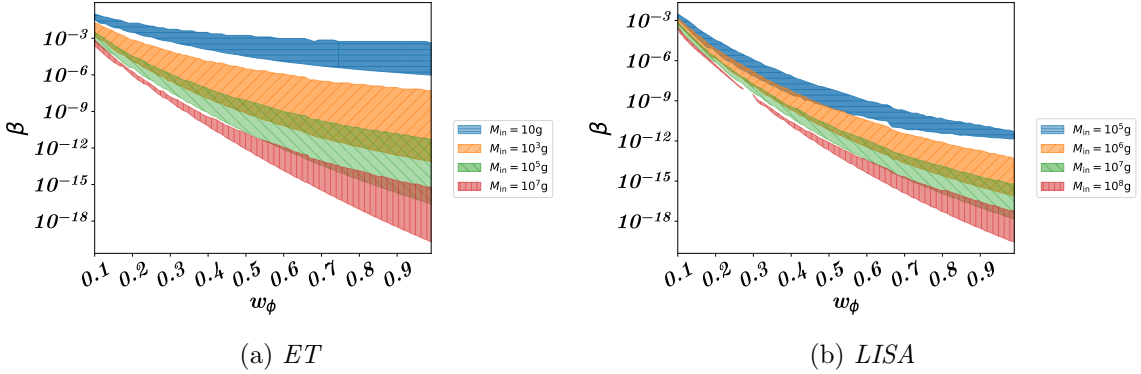


Figure 12: Illustration of extent of parameter space for various M_{in} where $\text{SNR} \geq 1$, considering GWs due to *adiabatic fluctuation*, for *ET* (left) and *LISA* (right). The upper limit comes from the GW overproduction, derived from ΔN_{eff} constraints at BBN.

Fisher matrix analysis:

In Figs. 13 and 14, we present the relative uncertainties in w_ϕ and β , respectively, for *ET*, considering $M_{\text{in}} = 10^5 \text{ g}$ and 10^7 g . Similarly, Figs. 15 and 16 illustrate the same analysis for *LISA*. A key finding of this Fisher analysis is that, for the adiabatic source, the relative uncertainties in w_ϕ and β , given by $\Delta w_\phi/w_\phi$ and $\Delta\beta/\beta$, are significantly smaller than 1. In contrast, for the isocurvature source, achieving $\Delta w_\phi/w_\phi$ or $\Delta\beta/\beta < 1$ is not feasible, which makes the detection of isocurvature source with higher uncertainty.

Notably, for both ET and LISA, in the high SNR region (*i.e.* $\text{SNR} > 1$), we find consistently low uncertainties (*i.e.* $\Delta w_\phi/w_\phi, \Delta\beta/\beta < 1$), reinforcing the idea that induced GWs from the adiabatic source can be measured with high precision. Thus, in agreement with the SNR analysis, the Fisher analysis further confirms that both LISA and ET are well-suited for detecting induced GWs from the adiabatic source with minimal uncertainties.

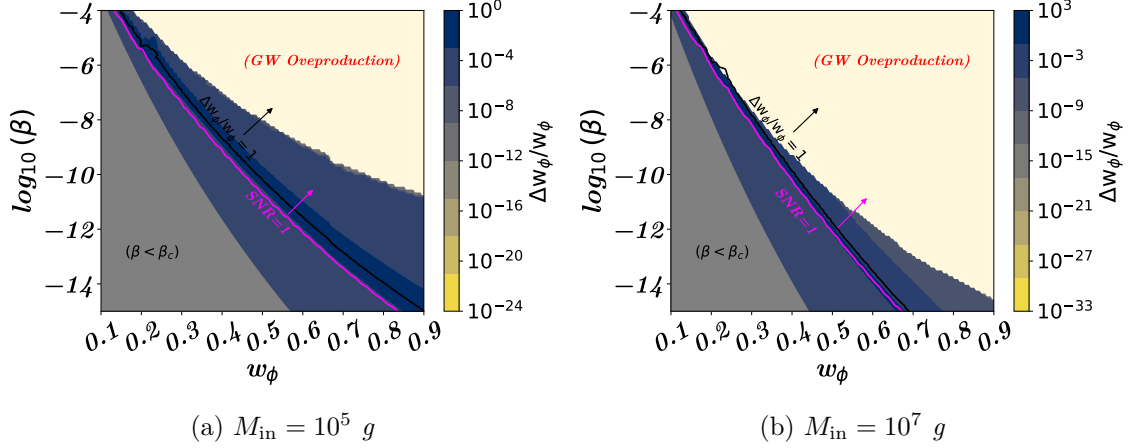


Figure 13: Illustration of relative uncertainties on w_ϕ , calculated by Fisher analysis, for the induced GWs from **adiabatic fluctuation** while considering **ET**. Black (magenta) solid line indicates $\text{SNR} = 1$ ($\Delta w_\phi/w_\phi = 1$). The black (magenta) arrow indicates where $\text{SNR} > 1$ ($\Delta w_\phi/w_\phi < 1$).

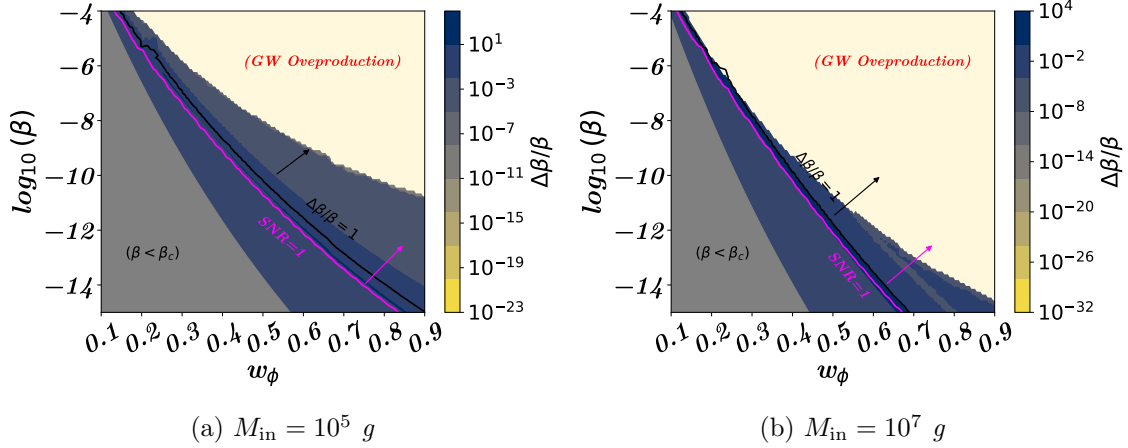


Figure 14: Representation is same as Fig. 13. However, it is the illustration of relative uncertainties on β , for **ET**.

5 Combined analysis with primordial source and PBH domination

The two sources of induced GWs are independent and contribute to the spectrum of the induced GWs simultaneously in the PBH reheating scenario. Consequently, the most realistic approach is to assess the detectability of the combined spectrum at the detectors.

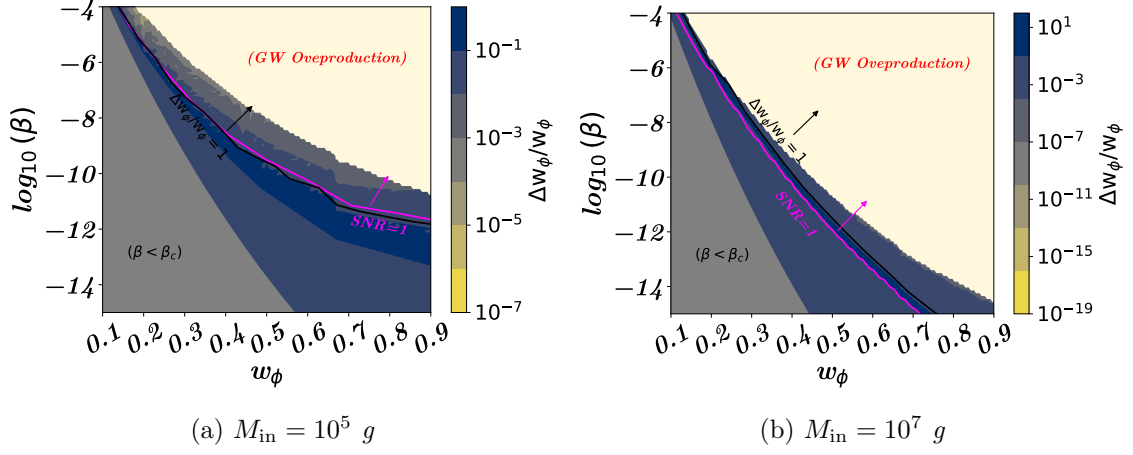


Figure 15: Figure is same as Fig. 13, but for *LISA*.

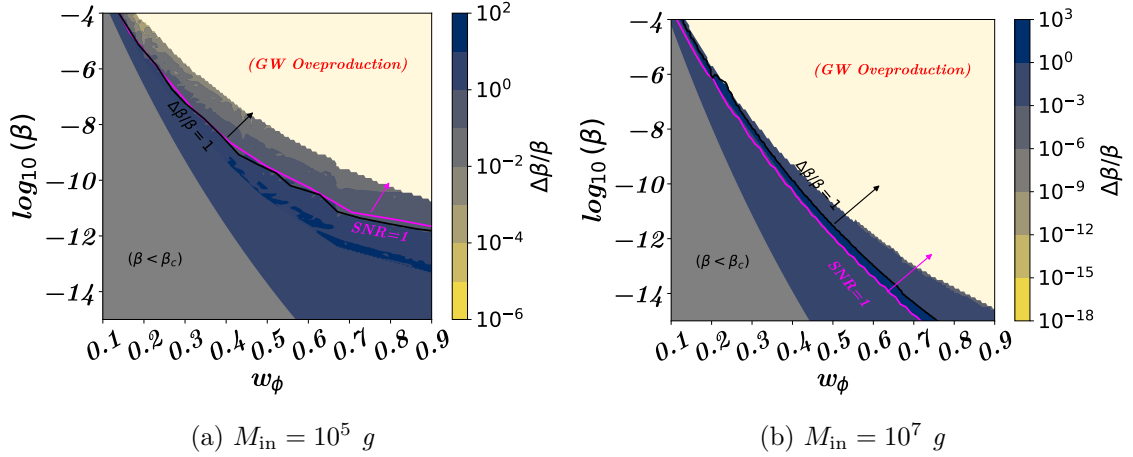


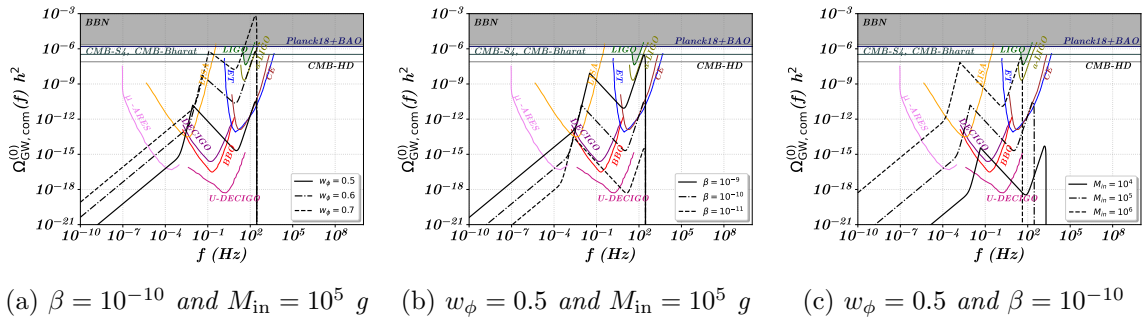
Figure 16: Figure is same as Fig. 13, but for relative uncertainties on β , considering *LISA*.

The resulting present-day energy density spectrum of the induced GWs can be expressed as

$$\Omega_{\text{GW,com}}^{(0)}(f)h^2 = \Omega_{\text{GW,iso}}^{(0)}(f)h^2 + \Omega_{\text{GW,ad}}^{(0)}(f)h^2. \quad (5.1)$$

This linear superposition arises from the statistical independence of the two sources, meaning their contributions add up without interference. Evaluating the detectability of $\Omega_{\text{GW,com}}^{(0)}(f)$ provides a more comprehensive understanding of the observational prospects for early Universe physics, particularly the PBH reheating scenario, in the light of future GW detectors.

The combined spectrum is illustrated in Fig. 17, highlighting the distinct contributions of the two sources. The induced GWs spectrum for adiabatic fluctuations peaks around k_{UV} (Fig. 9), whereas for the isocurvature scenario, it peaks at k_{BH} (Fig. 2). This results in two distinct peaks at characteristic frequencies, as shown in Fig. 17, enhancing the overall prospects for detection across a broader frequency range. This complimentary coverage may increase the likelihood that the combined spectrum could be probed by future GW observatories.



(a) $\beta = 10^{-10}$ and $M_{\text{in}} = 10^5 g$ (b) $w_\phi = 0.5$ and $M_{\text{in}} = 10^5 g$ (c) $w_\phi = 0.5$ and $\beta = 10^{-10}$

Figure 17: Induced gravitational wave spectrum at the present considering **combined sources**. Each of the plots are the presentation for the variation of the three parameters while the other two are kept fixed.

5.1 Statistical analysis in the light of the detectors

Since both the sources exhibit interesting prospects on their own merits, a combined statistical analysis of the combined spectrum is inevitable. As an example, for one source, the induced GWs may fall within the detection range, while for the other, an overproduction of GWs could make the scenario incompatible—an issue we will explore in detail in the next section. Therefore, a rigorous statistical analysis is essential for accurately estimating the parameters, which is presented in this section.

Evaluation of signal-to-noise ratio:

Similarly to the earlier study, we have estimated the SNR for ET and LISA in Figs. 18 and 19, respectively, for two representative values of M_{in} ($10^5 g$ and $10^7 g$). The other annotations and shaded regions have the same physical interpretation as before. Fig. 17 suggests that the peaks in the spectrum, originating from two different sources, dominate each other for different PBH parameters. Consequently, some of the parameter space may be reduced due to the overproduction of GWs compared to individual sources. This effect is evident by comparing the adiabatic scenario (Fig. 11a) with the combined scenario (Fig. 19a), where the $\text{SNR} > 1$ region in the $w_\phi - \beta$ plane shrinks in the combined case. To illustrate this effect, we have explicitly compared the GW overproduction limit of the combined spectrum with those from individual sources for different masses in Fig. 20, showing that the combined scenario follows a tighter limit than the individual sources.

Moreover, we have also represented the possible detectable range of parameters ($\text{SNR} \geq 1$) in the $w_\phi - \beta$ plane for distinct values of M_{in} in Fig. 21, considering two interferometric missions, ET and LISA, analogous to the earlier analysis. Notably, this is not simply a direct sum of the parameter spaces from the two individual sources; rather, we observe a reduction in the compatible parameter space in the $w_\phi - \beta$ plane. This effect is evident when comparing Fig. 21 with Figs. 12 and 4. This comparison demonstrates that, the combined scenario imposes tighter constraints than the individual sources, which is due to GW overproduction as we mentioned earlier.

An important point to note is the inherent degeneracy between the two sources, particularly in terms of SNR. This implies that, based on SNR alone, it is challenging to determine whether the stochastic gravitational wave signal originates from the adiabatic or isocurvature source. Resolving this degeneracy requires further investigation. In partic-

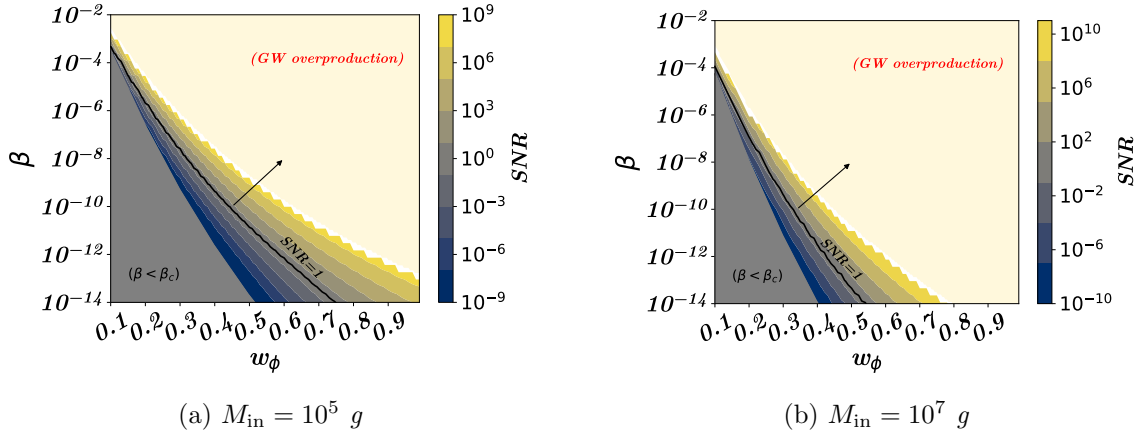


Figure 18: *SNR plots for **ET** considering two different values of M_{in} considering the combined sources. Rest of the illustration is same as Fig. 3.*

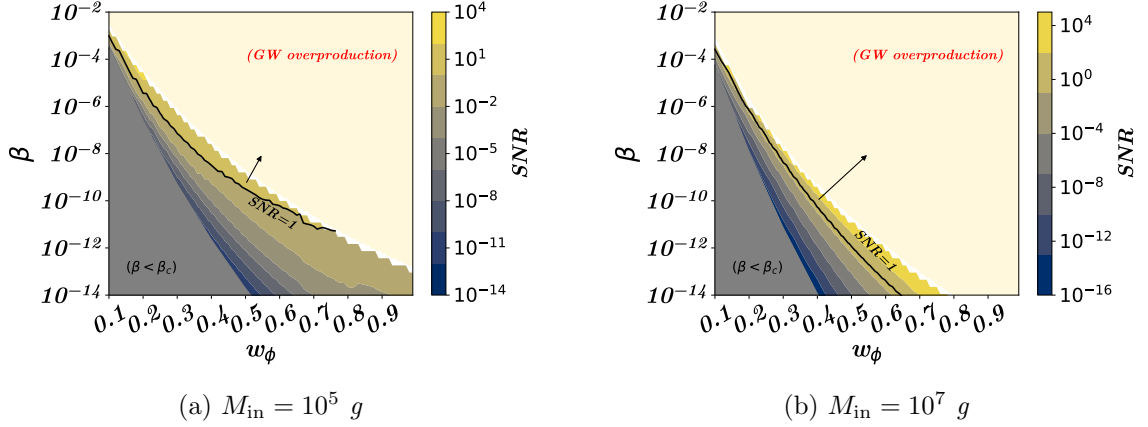


Figure 19: *Figure is same as Fig. 3, but for the combined sources, considering **LISA**.*

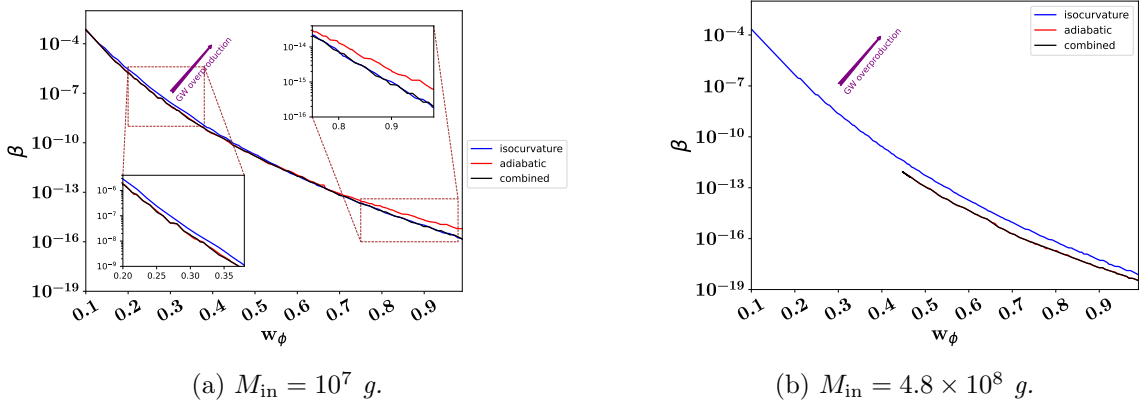


Figure 20: *Comparison of the maximum limit on the β parameter imposed by ΔN_{eff} constraints at BBN, considering induced GWs from three cases: isocurvature, adiabatic, and combined scenarios, for two distinct PBH formation masses.*

ular, once observational data becomes available, the spectral shape of the detected signal will be crucial in distinguishing between the two sources. The distinct peak structures and

frequency dependence of the adiabatic and isocurvature contributions, as discussed earlier, will play a key role in identifying the dominant mechanism responsible for the observed stochastic GWs background.

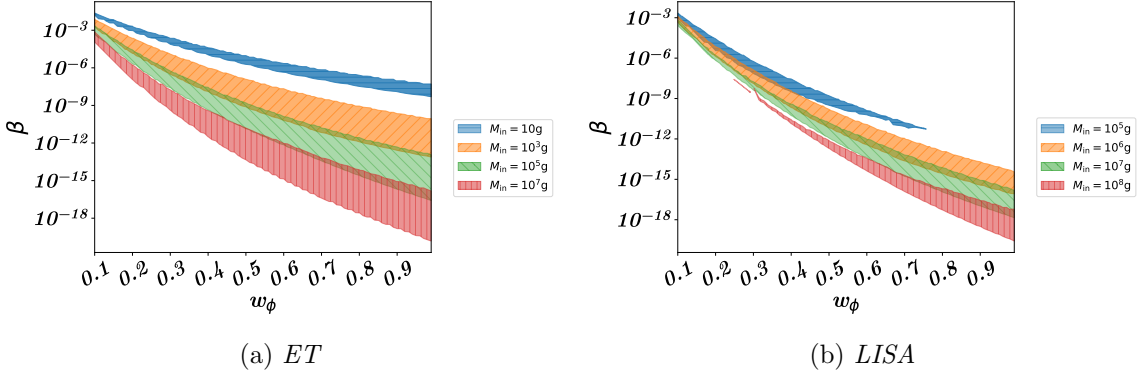


Figure 21: Illustration of extent of parameter space for various M_{in} where $\text{SNR} \geq 1$, considering *the combined sources of GWs*, for ET (left) and LISA (right). The upper limit comes from the GW overproduction, derived from ΔN_{eff} constraints at BBN.

Fisher matrix analysis:

Similar to the earlier sources, we have also performed the Fisher analysis to demonstrate the uncertainties on the parameters. Figs. 22 and 23 depict the forecasted uncertainties on w_ϕ and β , respectively, for ET, considering two representative values of M_{in} . Similarly, Figs. 24 and 25 present the corresponding results for LISA. As the uncertainties associated with the parameters are smaller for the adiabatic scenario, combined analysis predominantly follows the adiabatic case. However, as observed in the SNR results, the reduced parameter space due to GW overproduction-limit in the combined scenario also shrinks the regions with lower uncertainties. This effect can be clearly observed by comparing Fig. 24a with 15a, and 25a with 16a.

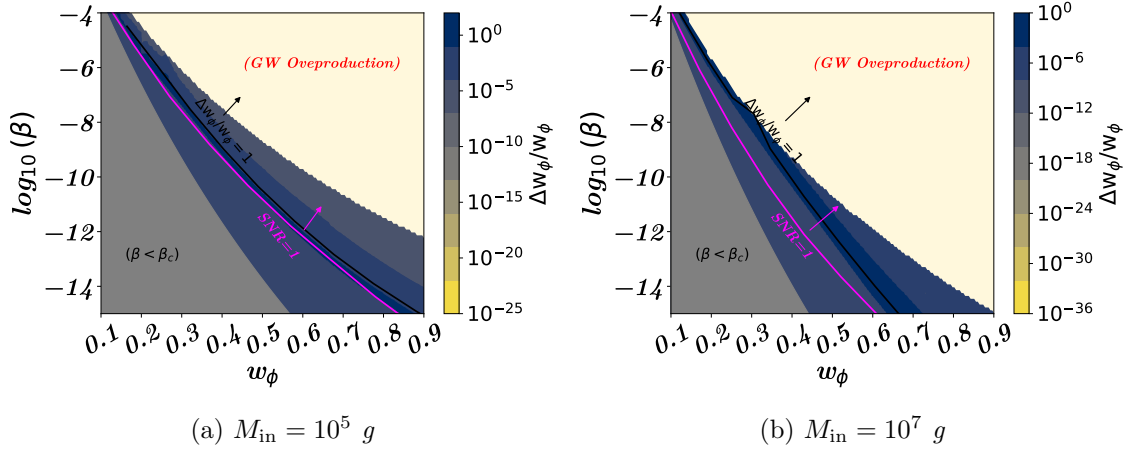


Figure 22: Illustration of relative uncertainties on w_ϕ , calculated by Fisher analysis, considering *combined sources of GWs* for ET. Black (magenta) solid line indicates $\text{SNR} = 1$ ($\Delta w_\phi / w_\phi = 1$). The black (magenta) arrow indicates where $\text{SNR} > 1$ ($\Delta w_\phi / w_\phi < 1$).

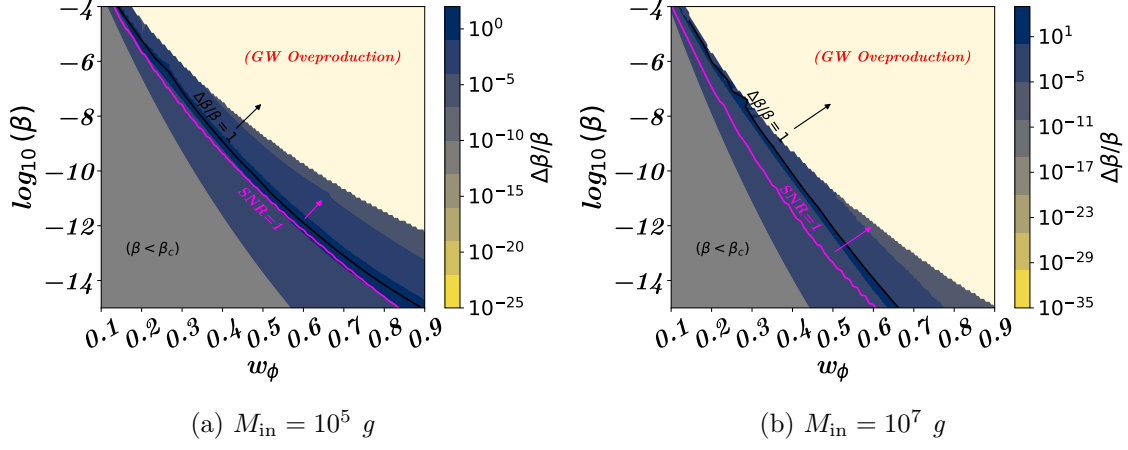


Figure 23: Representation is same as Fig. 22 but for relative uncertainties on β , considering *ET*.

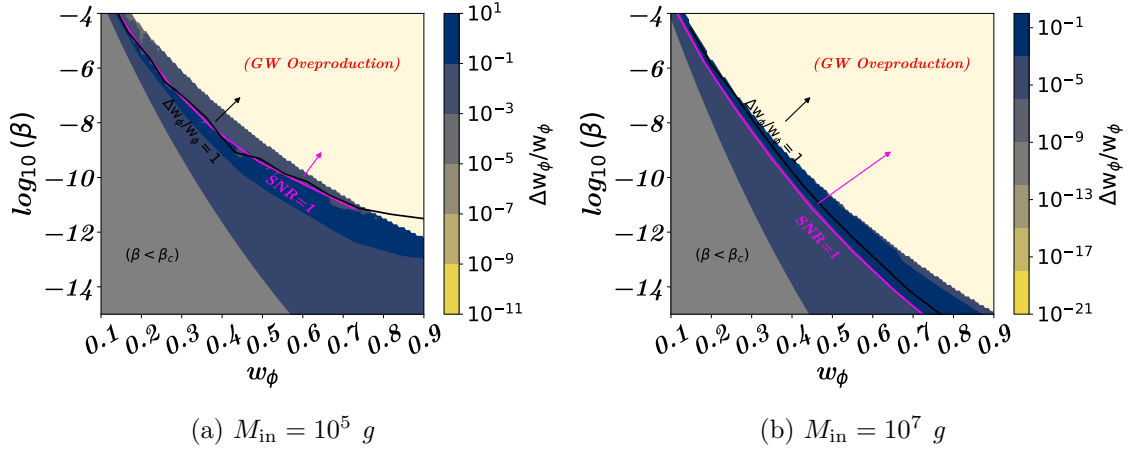


Figure 24: Figure is same as Fig. 22, but for *LISA*.

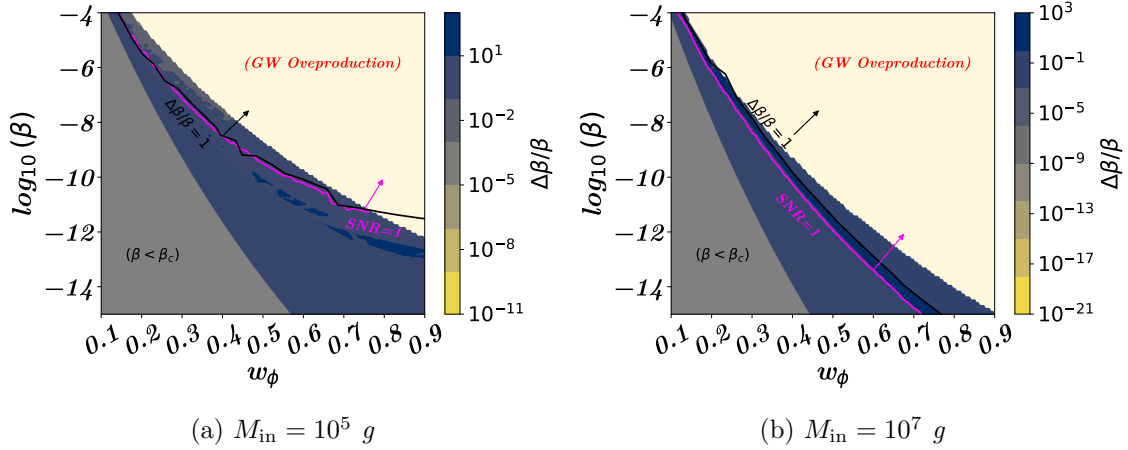


Figure 25: Figure is same as Fig. 22, but for relative uncertainties on β , considering *LISA*.

Accordingly, we have presented the posterior distribution of w_ϕ and β , derived from Fisher analysis, for $M_{\text{in}} = 10^5 g$ in Fig. 26, for both detectors. Fiducials with correspond-

ing uncertainties, for the other parameters, are tabulated in Table-3. The 2D posterior distribution depicts anti-correlation between w_ϕ and β . This trend of correlation is intuitive as both the parameters enhance the GW spectrum for the increasing values of them. Hence, for a given sensitivity threshold if w_ϕ is larger, β needs to be smaller. Furthermore, the results illustrate that the uncertainties are relatively smaller for ET compared to LISA. This may be an artefact of the following reasons: The instrumental noise for LISA is larger compared to ET (as evident from Fig. 28), and the frequency binning, N_b has been kept same for both detectors. However, as LISA operates over a broader frequency range than ET, Δf (defined in Sec. 3.2) is comparatively larger for LISA. This leads to larger uncertainties for LISA, as a larger Δf corresponds to smaller resolution of the detector.

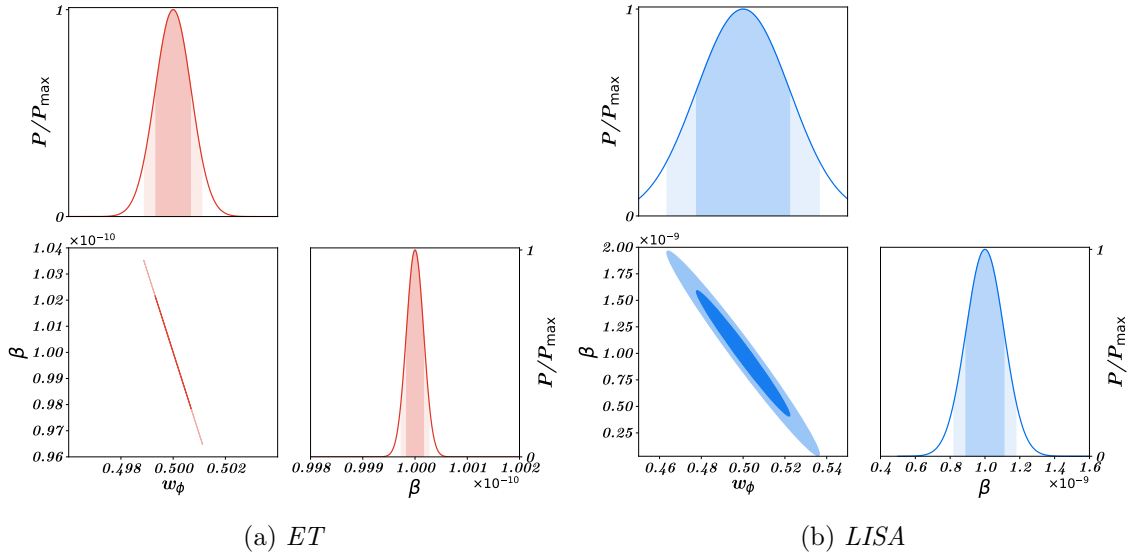


Figure 26: 1-D and 2-D posterior distribution, derived from Fisher analysis, considering the combined sources of GWs.

Parameter	Detectors	Fiducials	1- σ
w_ϕ	ET	0.5	0.0010
	LISA	0.5	0.0294
$\log_{10}(\beta)$	ET	-10	0.0160
	LISA	-9	0.3893

Table 3: Fiducials and corresponding 1- σ uncertainties associated with the parameters, derived from Fisher analysis, considering **combined scenario**. M_{in} is set to 10^5 g.

MCMC analysis with mock data:

Based on the basic setup described in Sec. 3.2, we have conducted the MCMC analysis for ET and LISA, considering the combined scenario, resulting in an estimation of the parameters under consideration using mock data generated from the instrumental specifications and possible sources of noise for both the missions. The priors adopted for the parameters are listed in Table-2. To generate the mock data, we have considered the fiducial parameter set by $(w_\phi, \log_{10}(\beta), \log_{10}(\frac{M_{\text{in}}}{1g})) \equiv (0.5, -9, 5)$ for both detectors. This choice ensures

that resulting GW spectrum satisfies $\text{SNR} > 1$ and relative uncertainties < 1 , for both detectors. Finally, the mock catalogue itself is generated following methodology outlined in Sec. 3.2. Using on the mock catalogues, we have presented 1- and 2-dimensional posterior distributions for ET and LISA in Fig. 27, with the corresponding statistical results summarized in Table-4.

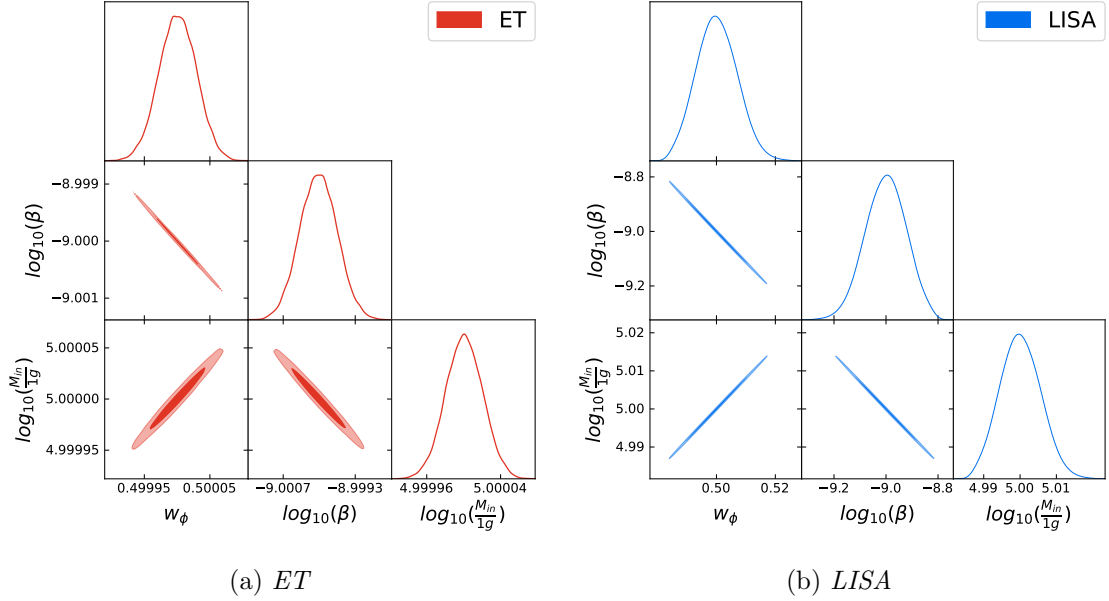


Figure 27: 1-D and 2-D posterior distribution for ET and LISA, considering three parameters associated with **combined scenario**.

Parameter	mean \pm σ	
	ET	LISA
w_ϕ	$0.5000^{+0.00004}_{-0.00004}$	$0.4995^{+0.0084}_{-0.0081}$
$\log_{10}(\beta)$	$-9.000^{+0.0005}_{-0.0005}$	$-8.995^{+0.0917}_{-0.0967}$
$\log_{10}(\frac{M_{\text{in}}}{1g})$	$5.000^{+0.00003}_{-0.00003}$	$5.000^{+0.0066}_{-0.0068}$

Table 4: Statistical results corresponding to the three parameters for each of the detectors, derived from MCMC analysis for **combined scenario**.

The posterior distributions reveal that $\log_{10}(\beta)$ exhibits a negative correlation with both w_ϕ and $\log_{10}(\frac{M_{\text{in}}}{1g})$, whereas w_ϕ and $\log_{10}(\frac{M_{\text{in}}}{1g})$ are positively correlated, for both detectors. This is fully consistent with the trends observed in the Fisher analysis, described earlier. Furthermore, Table-4 reveals that the uncertainties, associated with each of the parameters, are relatively less for ET compared to LISA, aligning with the findings from the Fisher analysis. As discussed previously, this is primarily due to the comparatively lower noise floor of ET and its lower Δf , representing finer resolution for ET compared to LISA.

6 Summary and outlook

In this study, we explored the generation of stochastic GWs produced during the PBH reheating epoch, focusing on two distinct sources: *isocurvature density fluctuations* from inhomogeneous spatial variations and *adiabatic primordial curvature perturbation*. These sources generate complementary induced GWs spectra, which fall within the sensitivity range of future interferometry missions, providing a unique probe of early Universe cosmology through GW detection. We have systematically analysed these two sources, first individually and then in combination, to explore the detection prospects of the relevant parameters ($w_\phi, \beta, M_{\text{in}}$) at future interferometry missions such as LISA and ET. Note that we assume the tensor-to-scalar ratio to be sufficiently small, ensuring that the impact of primary GWs—originating from tensor perturbations generated by vacuum fluctuations during inflation—remains negligible (see, for instance, Ref. [117, 118] for detection prospects of the early Universe in the context of primary GWs, considering future interferometry missions).

Below we summarize the key findings from our analysis.

- Isocurvature fluctuations:** Our analysis reveals distinct detection capabilities for two different interferometry missions, ET and LISA. While ET demonstrates strong sensitivity across a broad PBH mass range, $M_{\text{in}} \in (0.5 - 3.34 \times 10^7)$ g, LISA is only sensitive to PBH masses above 10^8 g. However, ET is not expected to detect the spectrum for PBHs with a formation mass exceeding 4×10^7 g, as the formation peak lies beyond its sensitivity range, highlighting a complementary detection window between LISA and ET. The parameter space in the $\beta - w_\phi$ plane is explored, constrained by the requirement $\text{SNR} > 1$ and limits from GW overproduction (*i.e.*, the ΔN_{eff} bound at BBN). One notable outcome is that the detectable region ($\text{SNR} > 1$) in the $\beta - w_\phi$ plane for ET is significantly large for a PBH formation mass around $M_{\text{in}} \sim 10^6$ g. This is expected, as the peak frequency, associated with the UV cutoff scale k_{UV} for the masses around 10^6 g, falls within the range where the noise spectrum $\Omega_{\text{GW}}^{\text{noise}}$ for ET attains its minimum. In contrast, for LISA, achieving $\text{SNR} > 1$ proves highly challenging, making it less favorable for detecting the isocurvature source of induced GWs.

Although for ET we found high SNR values considering isocurvature source, the precision in constraining the parameters remains relatively poor. Fisher analysis indicates that achieving relative uncertainties below 1 for both parameters, w_ϕ and β , is not possible for any PBH mass, with uncertainties exceeding 10 in most cases. The situation is even worse for LISA, where the SNR value is relatively low and the parameter uncertainties are significantly higher. Thus, while the GW spectrum induced by isocurvature fluctuations shows promising detection prospects, particularly for ET, the precision in constraining the underlying parameters remains low. As a result, although detection is feasible, accurately probing these parameters through either detector is unlikely for GWs induced by isocurvature fluctuations.

- Adiabatic fluctuations:** This spectrum spans a broader frequency range, significantly enhancing detection prospects. As in the previous scenario, ET is sensitive to PBH masses in the range $M_{\text{in}} \in (0.5 - 3.97 \times 10^7)$ g. However, the detection

prospects for LISA are notably improved in this case. SNR analysis suggests that for LISA, PBH masses within $M_{\text{in}} \in (2.3 \times 10^4 - 4.8 \times 10^8)$ g satisfy the condition $\text{SNR} > 1$, in contrast to the isocurvature case, where achieving a significant SNR proved highly challenging. Additionally, the extent of the detectable parameter space in the $\beta - w_\phi$ plane reaches its maximum around $M_{\text{in}} \sim 10^3$ g for ET, while for LISA, it is approximately 10^6 g.

Thus, both detectors are well-placed in terms of prospects of detection and constraining the parameters, with relative uncertainties often falling below 1 in regions where $\text{SNR} > 1$. This makes adiabatic-induced GWs a more promising probe of PBH reheating physics compared to the isocurvature case for both detectors.

- **Combined scenario:** When both sources contribute simultaneously—which is generally the case—neither can be ignored, the combined GWs spectrum remains detectable across the same mass ranges expected from both the adiabatic and isocurvature cases, with LISA and ET exhibiting complementary sensitivity. Table 5 summarizes the detectable ranges of M_{in} for all three types of sources. In the combined scenario, the extent of the parameter space in the $\beta - w_\phi$ plane that satisfies $\text{SNR} > 1$ is modified for both detectors (Fig. 21), primarily due to the overproduction of GWs, as constrained by the ΔN_{eff} bound from BBN (see, for instance, Fig. 20).

Like the adiabatic case, ET and LISA seem to have prospects of detecting as well as constraining the parameter with high precision. The posterior distributions for both Fisher analysis (Fig. 26) and MCMC analysis (Fig. 27) reveal a negative correlation between w_ϕ and β . Additionally, both statistical results infer that the uncertainties in probing the parameters are smaller for ET.

<i>Detectors</i>	<i>Isocurvature</i>	<i>Adiabatic</i>	<i>Combined</i>
ET	$(0.5 - 3.34 \times 10^7)$	$(0.5 - 3.97 \times 10^7)$	$(0.5 - 3.97 \times 10^7)$
LISA	$(2 \times 10^8 - 4.8 \times 10^8)$	$(2.3 \times 10^4 - 4.8 \times 10^8)$	$(2.3 \times 10^4 - 4.8 \times 10^8)$

Table 5: Detectable range of M_{in} for both source types and the combined case, in grams.

This study highlights the synergy of next-generation GW observatories, with LISA and ET offering complementary sensitivity across a broad PBH mass range. It also sheds light on the distinct nature of the two sources in terms of both detection and constraint prospects. However, we currently lack a mechanism to break the degeneracy between them. Once observational data becomes available, the spectral shape, distinct peak structures, and frequency dependence will be crucial in identifying the dominant source of the detected GW background. Detecting these induced GWs with LISA and ET could help distinguish between the two sources, providing valuable insights into the early Universe and the role of PBHs in GWs generation. This work underscores the importance of multi-signal searches in future GW data, demonstrating how stochastic backgrounds from non-standard early-Universe processes could serve as key cosmological messengers in the upcoming era of gravitational wave astronomy.

The analysis presented in the article can be extended further in a number of directions. This present analysis focuses only on Schwarzschild PBHs with a monochromatic mass

distribution. A key extension would be to explore spinning PBHs and an extended mass function, as both could significantly impact the induced GW spectrum. Understanding how an extended mass distribution influences the amplitude, peak frequency, and shape of the GW signal will be crucial for refining detection prospects. Additionally, our model-independent approach to PBH parameters can be further developed by linking constraints to specific formation mechanisms. Connecting induced GWs to scenarios like inflationary dynamics, cosmic strings, or phase transitions could provide deeper insights into early Universe physics.

On the observational front, next-generation detectors such as DECIGO and BBO, along with pulsar timing arrays (PTAs), could offer a multi-frequency probe of PBH-induced GWs. The synergy between space- and ground-based detectors will be essential for constraining PBH properties across different mass ranges. Furthermore, combining GW observations with multimessenger signals from the CMB, BBN, and high-energy astrophysics could provide a more comprehensive understanding of PBH reheating and early Universe dynamics.

A Noise modelling

For any GW detectors, the effective noise power spectral density, $S(f)$, can be expressed as the ratio of detector's response function $R(f)$ and noise $N(f)$. As a result, the noise curves for any GW detectors can be described as [105]:

$$\Omega_{\text{GW}}^{\text{noise}}(f) = \left(\frac{4\pi^2}{3H_0^2} \right) f^3 S(f). \quad (\text{A.1})$$

In the following, we discuss a summary of the $S(f)$ for the GW missions considered.

- **LISA**

The key sources of instrumental noise in LISA arises mainly due to be optical metrology noise (omn) and acceleration noise of the test mass (acc), resulting from disturbances of the test mass [105]. The contributions are expressed as following [119]:

$$S_{\text{acc}}(f) = 9 \times 10^{-30} \frac{1}{(2\pi f/1\text{Hz})^4} \left(1 + \frac{10^{-4}}{f/1\text{Hz}} \right) \text{ m}^2\text{Hz}^{-1}, \quad (\text{A.2})$$

$$S_{\text{oms}}(f) = (1.5 \times 10^{-11}\text{m})^2 \left[1 + \left(\frac{2\text{mHz}}{f} \right)^4 \right] \text{ Hz}^{-1}. \quad (\text{A.3})$$

Hence, the instrumental noise for the LISA reads as

$$S_{\text{LISA}}(f) = \frac{10}{3L^2} \left(2S_{\text{acc}}(f) \left(1 + \cos^2 \left(\frac{f}{c/(2\pi L)} \right) \right) + S_{\text{oms}}(f) \right) \left[1 + \frac{6}{10} \left(\frac{f}{c/(2\pi L)} \right)^2 \right], \quad (\text{A.4})$$

with $L = 2.5 \times 10^9$ m being the constellation arm-length of the instrument. Now the GW energy density power spectrum can be calculated from Eq. (A.1).

- **ET**

For ET we have followed Ref. [120] to generate the noise curve.

Fig. 28 represents the instrumental noise spectra for both detectors.

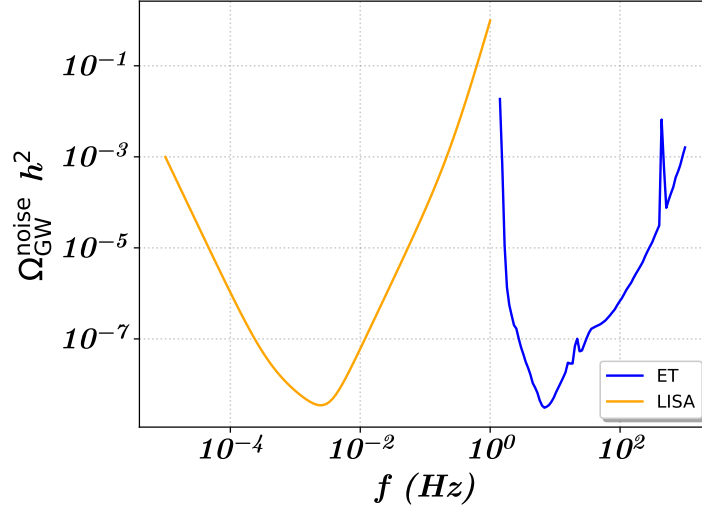


Figure 28: Noise spectra for LISA and ET.

B Calculation of cutoff function

For the isocurvature case, UV cutoff function ($\Theta_{\text{UV}}^{(\text{iso})}(k)$) for the resonant part, in Eq. (4.9), can be defined as [115]

$$\begin{aligned} \Theta_{\text{UV}}^{(\text{iso})}(k) &\equiv \int_{-s_0(k)}^{s_0(k)} ds \frac{(s^2 - 1)^2}{(1 - c_s^2 s^2)^{5/3}} \\ &= \frac{3s_0 (5c_s^4 - 2c_s^2 (2s_0^2 + 5) + 9) - (5c_s^2 (c_s^2 + 6) - 27) s_0 (c_s^2 s_0^2 - 1) {}_2F_1\left(\frac{5}{6}, 1; \frac{3}{2}; c_s^2 s_0^2\right)}{10c_s^4 (1 - c_s^2 s_0^2)^{2/3}}, \end{aligned} \quad (\text{B.1})$$

whereas for the adiabatic case, the cutoff function $\Theta_{\text{UV}}^{(\text{ad})}(k)$ for the resonant part for the adiabatic scenario, in Eq. (4.20), can be expressed as

$$\begin{aligned} \Theta_{\text{UV}}^{(\text{ad})}(k) &\equiv \int_{-s_0(k)}^{s_0(k)} ds (s^2 - 1)^2 (1 - c_s^2 s^2)^{n_{\text{eff}}(w_\phi)} \\ &= \frac{2}{5} s_0^5 {}_2F_1\left(\frac{5}{2}, -n_{\text{eff}}(w_\phi); \frac{7}{2}; c_s^2 s_0^2\right) - \frac{4}{3} s_0^3 {}_2F_1\left(\frac{3}{2}, -n_{\text{eff}}(w_\phi); \frac{5}{2}; c_s^2 s_0^2\right) \\ &\quad + 2s_0 {}_2F_1\left(\frac{1}{2}, -n_{\text{eff}}(w_\phi); \frac{3}{2}; c_s^2 s_0^2\right). \end{aligned} \quad (\text{B.2})$$

In the above two scenarios, $s_0(k)$ can be defined as

$$s_0(k) \equiv \begin{cases} 1 & \frac{k_{\text{UV}}}{k} \geq \frac{1+c_s^{-1}}{2} \\ 2\frac{k_{\text{UV}}}{k} - c_s^{-1} & \frac{1+c_s^{-1}}{2} \geq \frac{k_{\text{UV}}}{k} \geq \frac{c_s^{-1}}{2} \\ 0 & \frac{c_s^{-1}}{2} \geq \frac{k_{\text{UV}}}{k} \end{cases}. \quad (\text{B.3})$$

Acknowledgements

Authors sincerely thank Jan Tränkle and Guillem Doménech for their fruitful discussion. Authors also acknowledge the use of publicly available codes `emcee` [108] and `GetDist` [109], and thank the computational facilities of Technology Innovation Hub, ISI Kolkata and of

the Pegasus cluster of the high performance computing (HPC) facility at IUCAA, Pune. DP thanks ISI Kolkata for financial support through Senior Research Fellowship. MRH acknowledges ISI Kolkata for providing financial support through Research Associateship. SP thanks the ANRF, Govt. of India for partial support through Project No. CRG/2023/003984.

References

- [1] S. W. Hawking, *Black hole explosions*, *Nature* **248** (1974) 30.
- [2] B. J. Carr and S. W. Hawking, *Black holes in the early Universe*, *Mon. Not. Roy. Astron. Soc.* **168** (1974) 399.
- [3] S. W. Hawking, *Particle Creation by Black Holes*, *Commun. Math. Phys.* **43** (1975) 199. [Erratum: *Commun.Math.Phys.* 46, 206 (1976)].
- [4] LIGO SCIENTIFIC, VIRGO Collaboration, B. P. Abbott et al., *Observation of Gravitational Waves from a Binary Black Hole Merger*, *Phys. Rev. Lett.* **116** (2016) 061102 [[1602.03837](#)].
- [5] LIGO SCIENTIFIC, VIRGO Collaboration, B. P. Abbott et al., *GW151226: Observation of Gravitational Waves from a 22-Solar-Mass Binary Black Hole Coalescence*, *Phys. Rev. Lett.* **116** (2016) 241103 [[1606.04855](#)].
- [6] LIGO SCIENTIFIC, VIRGO Collaboration, B. P. Abbott et al., *GW170104: Observation of a 50-Solar-Mass Binary Black Hole Coalescence at Redshift 0.2*, *Phys. Rev. Lett.* **118** (2017) 221101 [[1706.01812](#)]. [Erratum: *Phys.Rev.Lett.* 121, 129901 (2018)].
- [7] LIGO SCIENTIFIC, VIRGO Collaboration, B. . P. . Abbott et al., *GW170608: Observation of a 19-solar-mass Binary Black Hole Coalescence*, *Astrophys. J. Lett.* **851** (2017) L35 [[1711.05578](#)].
- [8] LIGO SCIENTIFIC, VIRGO Collaboration, B. P. Abbott et al., *GW170814: A Three-Detector Observation of Gravitational Waves from a Binary Black Hole Coalescence*, *Phys. Rev. Lett.* **119** (2017) 141101 [[1709.09660](#)].
- [9] LIGO SCIENTIFIC, VIRGO Collaboration, B. P. Abbott et al., *GW170817: Observation of Gravitational Waves from a Binary Neutron Star Inspiral*, *Phys. Rev. Lett.* **119** (2017) 161101 [[1710.05832](#)].
- [10] B. J. Carr and J. E. Lidsey, *Primordial black holes and generalized constraints on chaotic inflation*, *Phys. Rev. D* **48** (1993) 543.
- [11] P. Ivanov, P. Naselsky and I. Novikov, *Inflation and primordial black holes as dark matter*, *Phys. Rev. D* **50** (1994) 7173.
- [12] J. Yokoyama, *Chaotic new inflation and formation of primordial black holes*, *Phys. Rev. D* **58** (1998) 083510 [[astro-ph/9802357](#)].
- [13] R. Saito, J. Yokoyama and R. Nagata, *Single-field inflation, anomalous enhancement of superhorizon fluctuations, and non-Gaussianity in primordial black hole formation*, *JCAP* **06** (2008) 024 [[0804.3470](#)].
- [14] J. Garcia-Bellido and E. Ruiz Morales, *Primordial black holes from single field models of inflation*, *Phys. Dark Univ.* **18** (2017) 47 [[1702.03901](#)].
- [15] J. Yokoyama, *Formation of MACHO primordial black holes in inflationary cosmology*, *Astron. Astrophys.* **318** (1997) 673 [[astro-ph/9509027](#)].
- [16] L. Randall, M. Soljatic and A. H. Guth, *Supernatural inflation: Inflation from supersymmetry with no (very) small parameters*, *Nucl. Phys. B* **472** (1996) 377 [[hep-ph/9512439](#)].

- [17] J. Garcia-Bellido, A. D. Linde and D. Wands, *Density perturbations and black hole formation in hybrid inflation*, *Phys. Rev. D* **54** (1996) 6040 [[astro-ph/9605094](#)].
- [18] S. Pi, Y.-l. Zhang, Q.-G. Huang and M. Sasaki, *Scalaron from R^2 -gravity as a heavy field*, *JCAP* **05** (2018) 042 [[1712.09896](#)].
- [19] J. H. MacGibbon and B. R. Webber, *Quark and gluon jet emission from primordial black holes: The instantaneous spectra*, *Phys. Rev. D* **41** (1990) 3052.
- [20] A. C. Jenkins and M. Sakellariadou, *Primordial black holes from cusp collapse on cosmic strings*, [2006.16249](#).
- [21] T. Helfer, J. C. Aurrekoetxea and E. A. Lim, *Cosmic String Loop Collapse in Full General Relativity*, *Phys. Rev. D* **99** (2019) 104028 [[1808.06678](#)].
- [22] T. Matsuda, *Primordial black holes from cosmic necklaces*, *JHEP* **04** (2006) 017 [[hep-ph/0509062](#)].
- [23] M. Lake, S. Thomas and J. Ward, *String Necklaces and Primordial Black Holes from Type IIB Strings*, *JHEP* **12** (2009) 033 [[0906.3695](#)].
- [24] S. G. Rubin, M. Y. Khlopov and A. S. Sakharov, *Primordial black holes from nonequilibrium second order phase transition*, *Grav. Cosmol.* **6** (2000) 51 [[hep-ph/0005271](#)].
- [25] S. G. Rubin, A. S. Sakharov and M. Y. Khlopov, *The Formation of primary galactic nuclei during phase transitions in the early universe*, *J. Exp. Theor. Phys.* **91** (2001) 921 [[hep-ph/0106187](#)].
- [26] H. Kodama, M. Sasaki and K. Sato, *Abundance of Primordial Holes Produced by Cosmological First-Order Phase Transition*, *Progress of Theoretical Physics* **68** (1982) 1979.
- [27] Y. Lu, Z. S. C. Picker, S. Profumo and A. Kusenko, *Black Holes from Fermi Ball Collapse*, [2411.17074](#).
- [28] Y. Lu, Z. S. C. Picker and A. Kusenko, *Direct Collapse Supermassive Black Holes from Relic Particle Decay*, *Phys. Rev. Lett.* **133** (2024) 091001 [[2404.03909](#)].
- [29] M. M. Flores, A. Kusenko and M. Sasaki, *Revisiting formation of primordial black holes in a supercooled first-order phase transition*, *Phys. Rev. D* **110** (2024) 015005 [[2402.13341](#)].
- [30] M. M. Flores, Y. Lu and A. Kusenko, *Structure formation after reheating: Supermassive primordial black holes and Fermi ball dark matter*, *Phys. Rev. D* **108** (2023) 123511 [[2308.09094](#)].
- [31] M. M. Flores and A. Kusenko, *New ideas on the formation and astrophysical detection of primordial black holes*, [2404.05430](#).
- [32] G. Ballesteros, J. Iguaz Juan, P. D. Serpico and M. Taoso, *Primordial black hole formation from self-resonant preheating?*, [2406.09122](#).
- [33] M. Drewes, J. U. Kang and U. R. Mun, *CMB constraints on the inflaton couplings and reheating temperature in α -attractor inflation*, *JHEP* **11** (2017) 072 [[1708.01197](#)].
- [34] M. A. G. Garcia, K. Kaneta, Y. Mambrini and K. A. Olive, *Reheating and Post-inflationary Production of Dark Matter*, *Phys. Rev. D* **101** (2020) 123507 [[2004.08404](#)].
- [35] M. R. Haque, D. Maity and P. Saha, *Two-phase reheating: CMB constraints on inflation and dark matter phenomenology*, *Phys. Rev. D* **102** (2020) 083534 [[2009.02794](#)].
- [36] M. A. G. Garcia, K. Kaneta, Y. Mambrini and K. A. Olive, *Inflaton Oscillations and Post-Inflationary Reheating*, *JCAP* **04** (2021) 012 [[2012.10756](#)].
- [37] M. R. Haque and D. Maity, *Gravitational reheating*, *Phys. Rev. D* **107** (2023) 043531 [[2201.02348](#)].

- [38] S. Clery, Y. Mambrini, K. A. Olive and S. Verner, *Gravitational portals in the early Universe*, *Phys. Rev. D* **105** (2022) 075005 [[2112.15214](#)].
- [39] S. Clery, Y. Mambrini, K. A. Olive, A. Shkerin and S. Verner, *Gravitational portals with nonminimal couplings*, *Phys. Rev. D* **105** (2022) 095042 [[2203.02004](#)].
- [40] R. T. Co, Y. Mambrini and K. A. Olive, *Inflationary gravitational leptogenesis*, *Phys. Rev. D* **106** (2022) 075006 [[2205.01689](#)].
- [41] A. Ahmed, B. Grzadkowski and A. Socha, *Higgs boson induced reheating and ultraviolet frozen-in dark matter*, *JHEP* **02** (2023) 196 [[2207.11218](#)].
- [42] M. R. Haque, D. Maity and R. Mondal, *Gravitational neutrino reheating*, *Phys. Rev. D* **109** (2024) 063543 [[2311.07684](#)].
- [43] J. C. Hidalgo, L. A. Urena-Lopez and A. R. Liddle, *Unification models with reheating via Primordial Black Holes*, *Phys. Rev. D* **85** (2012) 044055 [[1107.5669](#)].
- [44] J. Martin, T. Papanikolaou and V. Vennin, *Primordial black holes from the preheating instability in single-field inflation*, *JCAP* **01** (2020) 024 [[1907.04236](#)].
- [45] D. Hooper, G. Krnjaic and S. D. McDermott, *Dark Radiation and Superheavy Dark Matter from Black Hole Domination*, *JHEP* **08** (2019) 001 [[1905.01301](#)].
- [46] D. Hooper, G. Krnjaic, J. March-Russell, S. D. McDermott and R. Petrossian-Byrne, *Hot Gravitons and Gravitational Waves From Kerr Black Holes in the Early Universe*, [2004.00618](#).
- [47] D. Hooper and G. Krnjaic, *GUT Baryogenesis With Primordial Black Holes*, *Phys. Rev. D* **103** (2021) 043504 [[2010.01134](#)].
- [48] N. Bernal and O. Zapata, *Dark Matter in the Time of Primordial Black Holes*, *JCAP* **03** (2021) 015 [[2011.12306](#)].
- [49] A. Cheek, L. Heurtier, Y. F. Perez-Gonzalez and J. Turner, *Primordial black hole evaporation and dark matter production. II. Interplay with the freeze-in or freeze-out mechanism*, *Phys. Rev. D* **105** (2022) 015023 [[2107.00016](#)].
- [50] A. Cheek, L. Heurtier, Y. F. Perez-Gonzalez and J. Turner, *Evaporation of primordial black holes in the early Universe: Mass and spin distributions*, *Phys. Rev. D* **108** (2023) 015005 [[2212.03878](#)].
- [51] K. Mazde and L. Visinelli, *The interplay between the dark matter axion and primordial black holes*, *JCAP* **01** (2023) 021 [[2209.14307](#)].
- [52] M. Riajul Haque, E. Kpatcha, D. Maity and Y. Mambrini, *Primordial black hole reheating*, *Phys. Rev. D* **108** (2023) 063523 [[2305.10518](#)].
- [53] R. Calabrese, M. Chianese, J. Gunn, G. Miele, S. Morisi and N. Saviano, *Limits on light primordial black holes from high-scale leptogenesis*, *Phys. Rev. D* **107** (2023) 123537 [[2305.13369](#)].
- [54] B. Barman, S. Jyoti Das, M. R. Haque and Y. Mambrini, *A Gravitational Ménage à Trois: leptogenesis, primordial gravitational wave & PBH-induced reheating*, [2403.05626](#).
- [55] T. Papanikolaou, V. Vennin and D. Langlois, *Gravitational waves from a universe filled with primordial black holes*, *JCAP* **03** (2021) 053 [[2010.11573](#)].
- [56] G. Domènech, C. Lin and M. Sasaki, *Gravitational wave constraints on the primordial black hole dominated early universe*, *JCAP* **04** (2021) 062 [[2012.08151](#)]. [Erratum: *JCAP* **11**, E01 (2021)].
- [57] I. Dalianis and C. Kouvaris, *Gravitational waves from density perturbations in an early matter domination era*, *JCAP* **07** (2021) 046 [[2012.09255](#)].

- [58] G. Domènech, *Scalar Induced Gravitational Waves Review*, *Universe* **7** (2021) 398 [2109.01398].
- [59] G. Domènech, V. Takhistov and M. Sasaki, *Exploring evaporating primordial black holes with gravitational waves*, *Phys. Lett. B* **823** (2021) 136722 [2105.06816].
- [60] T. Papanikolaou, C. Tzerefos, S. Basilakos and E. N. Saridakis, *Scalar induced gravitational waves from primordial black hole Poisson fluctuations in $f(R)$ gravity*, *JCAP* **10** (2022) 013 [2112.15059].
- [61] N. Bhaumik, A. Ghoshal and M. Lewicki, *Doubly peaked induced stochastic gravitational wave background: testing baryogenesis from primordial black holes*, *JHEP* **07** (2022) 130 [2205.06260].
- [62] N. Bhaumik, A. Ghoshal, R. K. Jain and M. Lewicki, *Distinct signatures of spinning PBH domination and evaporation: doubly peaked gravitational waves, dark relics and CMB complementarity*, *JHEP* **05** (2023) 169 [2212.00775].
- [63] T. Papanikolaou, *Gravitational waves induced from primordial black hole fluctuations: the effect of an extended mass function*, *JCAP* **10** (2022) 089 [2207.11041].
- [64] N. Bhaumik, M. R. Haque, R. K. Jain and M. Lewicki, *Memory burden effect mimics reheating signatures on SGWB from ultra-low mass PBH domination*, *JHEP* **10** (2024) 142 [2409.04436].
- [65] G. Domènech and J. Tränkle, *From formation to evaporation: Induced gravitational wave probes of the primordial black hole reheating scenario*, 2409.12125.
- [66] K. Inomata, M. Kawasaki, K. Mukaida, T. Terada and T. T. Yanagida, *Gravitational Wave Production right after a Primordial Black Hole Evaporation*, *Phys. Rev. D* **101** (2020) 123533 [2003.10455].
- [67] G. White, L. Pearce, D. Vagie and A. Kusenko, *Detectable Gravitational Wave Signals from Affleck-Dine Baryogenesis*, *Phys. Rev. Lett.* **127** (2021) 181601 [2105.11655].
- [68] N. Bhaumik, R. K. Jain and M. Lewicki, *Ultralow mass primordial black holes in the early Universe can explain the pulsar timing array signal*, *Phys. Rev. D* **108** (2023) 123532 [2308.07912].
- [69] G. Bertone et al., *Gravitational wave probes of dark matter: challenges and opportunities*, *SciPost Phys. Core* **3** (2020) 007 [1907.10610].
- [70] P. Amaro-Seoane, H. Audley and S. B. et al., *Laser interferometer space antenna*, 2017.
- [71] J. Baker et al., *The Laser Interferometer Space Antenna: Unveiling the Millihertz Gravitational Wave Sky*, 1907.06482.
- [72] F. A. e. a. M. Punturo, M. Abernathy, *The einstein telescope: a third-generation gravitational wave observatory*, *Classical and Quantum Gravity* **27** (2010) 194002.
- [73] S. Hild et al., *Sensitivity Studies for Third-Generation Gravitational Wave Observatories*, *Class. Quant. Grav.* **28** (2011) 094013 [1012.0908].
- [74] A. Escrivà, C. Germani and R. K. Sheth, *Analytical thresholds for black hole formation in general cosmological backgrounds*, *JCAP* **01** (2021) 030 [2007.05564].
- [75] A. Arbey and J. Auffinger, *BlackHawk: A public code for calculating the Hawking evaporation spectra of any black hole distribution*, *Eur. Phys. J. C* **79** (2019) 693 [1905.04268].
- [76] A. Cheek, L. Heurtier, Y. F. Perez-Gonzalez and J. Turner, *Primordial black hole evaporation and dark matter production. I. Solely Hawking radiation*, *Phys. Rev. D* **105** (2022) 015022 [2107.00013].

- [77] I. Baldes, Q. Decant, D. C. Hooper and L. Lopez-Honorez, *Non-Cold Dark Matter from Primordial Black Hole Evaporation*, *JCAP* **08** (2020) 045 [[2004.14773](#)].
- [78] I. Musco and J. C. Miller, *Primordial black hole formation in the early universe: critical behaviour and self-similarity*, *Class. Quant. Grav.* **30** (2013) 145009 [[1201.2379](#)].
- [79] I. Musco, J. C. Miller and A. G. Polnarev, *Primordial black hole formation in the radiative era: Investigation of the critical nature of the collapse*, *Class. Quant. Grav.* **26** (2009) 235001 [[0811.1452](#)].
- [80] I. Hawke and J. M. Stewart, *The dynamics of primordial black hole formation*, *Class. Quant. Grav.* **19** (2002) 3687.
- [81] J. C. Niemeyer and K. Jedamzik, *Near-critical gravitational collapse and the initial mass function of primordial black holes*, *Phys. Rev. Lett.* **80** (1998) 5481 [[astro-ph/9709072](#)].
- [82] A. Escrivà and A. E. Romano, *Effects of the shape of curvature peaks on the size of primordial black holes*, *JCAP* **05** (2021) 066 [[2103.03867](#)].
- [83] A. Escrivà, *Simulation of primordial black hole formation using pseudo-spectral methods*, *Phys. Dark Univ.* **27** (2020) 100466 [[1907.13065](#)].
- [84] A. Escrivà, *PBH Formation from Spherically Symmetric Hydrodynamical Perturbations: A Review*, *Universe* **8** (2022) 66 [[2111.12693](#)].
- [85] M. R. Haque, E. Kpatcha, D. Maity and Y. Mambrini, *Primordial black hole versus inflaton*, *Phys. Rev. D* **109** (2024) 023521.
- [86] M. Kawasaki, K. Kohri and N. Sugiyama, *Cosmological constraints on late time entropy production*, *Phys. Rev. Lett.* **82** (1999) 4168 [[astro-ph/9811437](#)].
- [87] M. Kawasaki, K. Kohri and N. Sugiyama, *MeV scale reheating temperature and thermalization of neutrino background*, *Phys. Rev. D* **62** (2000) 023506 [[astro-ph/0002127](#)].
- [88] T. Hasegawa, N. Hiroshima, K. Kohri, R. S. L. Hansen, T. Tram and S. Hannestad, *MeV-scale reheating temperature and thermalization of oscillating neutrinos by radiative and hadronic decays of massive particles*, *JCAP* **12** (2019) 012 [[1908.10189](#)].
- [89] BICEP, KECK Collaboration, P. A. R. Ade et al., *Improved Constraints on Primordial Gravitational Waves using Planck, WMAP, and BICEP/Keck Observations through the 2018 Observing Season*, *Phys. Rev. Lett.* **127** (2021) 151301 [[2110.00483](#)].
- [90] BICEP2, PLANCK Collaboration, P. A. R. Ade et al., *Joint Analysis of BICEP2/KeckArray and Planck Data*, *Phys. Rev. Lett.* **114** (2015) 101301 [[1502.00612](#)].
- [91] D. Baumann, P. J. Steinhardt, K. Takahashi and K. Ichiki, *Gravitational Wave Spectrum Induced by Primordial Scalar Perturbations*, *Phys. Rev. D* **76** (2007) 084019 [[hep-th/0703290](#)].
- [92] J. R. Espinosa, D. Racco and A. Riotto, *A Cosmological Signature of the SM Higgs Instability: Gravitational Waves*, *JCAP* **09** (2018) 012 [[1804.07732](#)].
- [93] G. Domènech, *Induced gravitational waves in a general cosmological background*, *Int. J. Mod. Phys. D* **29** (2020) 2050028 [[1912.05583](#)].
- [94] H. V. Ragavendra, P. Saha, L. Sriramkumar and J. Silk, *Primordial black holes and secondary gravitational waves from ultraslow roll and punctuated inflation*, *Phys. Rev. D* **103** (2021) 083510 [[2008.12202](#)].
- [95] K. Inomata, K. Kohri and T. Terada, *Detected stochastic gravitational waves and subsolar-mass primordial black holes*, *Phys. Rev. D* **109** (2024) 063506 [[2306.17834](#)].

- [96] G. Franciolini, A. Iovino, Junior., V. Vaskonen and H. Veermae, *Recent Gravitational Wave Observation by Pulsar Timing Arrays and Primordial Black Holes: The Importance of Non-Gaussianities*, *Phys. Rev. Lett.* **131** (2023) 201401 [[2306.17149](#)].
- [97] H. Firouzjahi and A. Talebian, *Induced gravitational waves from ultra slow-roll inflation and pulsar timing arrays observations*, *JCAP* **10** (2023) 032 [[2307.03164](#)].
- [98] S. Maity, N. Bhaumik, M. R. Haque, D. Maity and L. Sriramkumar, *Constraining the history of reheating with the NANOGrav 15-year data*, [2403.16963](#).
- [99] T. Fujita, M. Kawasaki, K. Harigaya and R. Matsuda, *Baryon asymmetry, dark matter, and density perturbation from primordial black holes*, *Phys. Rev. D* **89** (2014) 103501 [[1401.1909](#)].
- [100] T. Papanikolaou, C. Tzerefos, S. Basilakos and E. N. Saridakis, *No constraints for $f(T)$ gravity from gravitational waves induced from primordial black hole fluctuations*, *Eur. Phys. J. C* **83** (2023) 31 [[2205.06094](#)].
- [101] T. Papanikolaou, X.-C. He, X.-H. Ma, Y.-F. Cai, E. N. Saridakis and M. Sasaki, *New probe of non-Gaussianities with primordial black hole induced gravitational waves*, [2403.00660](#).
- [102] K. Inomata, K. Kohri, T. Nakama and T. Terada, *Enhancement of Gravitational Waves Induced by Scalar Perturbations due to a Sudden Transition from an Early Matter Era to the Radiation Era*, *Phys. Rev. D* **100** (2019) 043532 [[1904.12879](#)]. [Erratum: Phys.Rev.D 108, 049901 (2023)].
- [103] E. Thrane and J. D. Romano, *Sensitivity curves for searches for gravitational-wave backgrounds*, *Phys. Rev. D* **88** (2013) 124032 [[1310.5300](#)].
- [104] C. Caprini et al., *Science with the space-based interferometer eLISA. II: Gravitational waves from cosmological phase transitions*, *JCAP* **04** (2016) 001 [[1512.06239](#)].
- [105] C. Gowling and M. Hindmarsh, *Observational prospects for phase transitions at LISA: Fisher matrix analysis*, *JCAP* **10** (2021) 039 [[2106.05984](#)].
- [106] S. Dodelson, *Modern Cosmology*. Academic Press, Amsterdam, 2003.
- [107] J. Ferreira, T. Barreiro, J. Mimoso and N. J. Nunes, *Forecasting $F(Q)$ cosmology with Λ CDM background using standard sirens*, *Phys. Rev. D* **105** (2022) 123531 [[2203.13788](#)].
- [108] D. Foreman-Mackey, D. W. Hogg, D. Lang and J. Goodman, *emcee: The MCMC Hammer*, *Publications of the Astronomical Society of the Pacific* **125** (2013) 306 [[1202.3665](#)].
- [109] A. Lewis, *GetDist: a Python package for analysing Monte Carlo samples*, [1910.13970](#).
- [110] K. Ando, K. Inomata and M. Kawasaki, *Primordial black holes and uncertainties in the choice of the window function*, *Phys. Rev. D* **97** (2018) 103528 [[1802.06393](#)].
- [111] K. Kohri and T. Terada, *Semianalytic calculation of gravitational wave spectrum nonlinearly induced from primordial curvature perturbations*, *Phys. Rev. D* **97** (2018) 123532 [[1804.08577](#)].
- [112] K. Inomata, K. Kohri, T. Nakama and T. Terada, *Enhancement of gravitational waves induced by scalar perturbations due to a sudden transition from an early matter era to the radiation era*, *Phys. Rev. D* **100** (2019) 043532 [[1904.12879](#)].
- [113] T. Papanikolaou, V. Vennin and D. Langlois, *Gravitational waves from a universe filled with primordial black holes*, *JCAP* **2021** (2021) 053 [[2010.11573](#)].
- [114] G. Domènech, C. Lin and M. Sasaki, *Gravitational wave constraints on the primordial black hole dominated early universe*, *JCAP* **2021** (2021) 062 [[2012.08151](#)].

- [115] G. Domènech and J. Tränkle, *From formation to evaporation: Induced gravitational wave probes of the primordial black hole reheating scenario*, [arXiv e-prints \(2024\)](#) [arXiv:2409.12125](#) [[2409.12125](#)].
- [116] PLANCK Collaboration, N. Aghanim et al., *Planck 2018 results. VI. Cosmological parameters*, *Astron. Astrophys.* **641** (2020) A6 [[1807.06209](#)]. [Erratum: *Astron. Astrophys.* 652, C4 (2021)].
- [117] A. Ghoshal, D. Paul and S. Pal, *Primordial Gravitational Waves as Probe of Dark Matter in Interferometer Missions: Fisher Forecast and MCMC*, [2405.06741](#).
- [118] S. Maity and M. R. Haque, *Probing the early universe with future GW observatories*, [2407.18246](#).
- [119] M. Breitbach, J. Kopp, E. Madge, T. Opferkuch and P. Schwaller, *Dark, Cold, and Noisy: Constraining Secluded Hidden Sectors with Gravitational Waves*, *JCAP* **07** (2019) 007 [[1811.11175](#)].
- [120] D. Chowdhury, G. Tasinato and I. Zavala, *Response of the Einstein Telescope to Doppler anisotropies*, *Phys. Rev. D* **107** (2023) 083516 [[2209.05770](#)].